# Non-circular cavity expansion in undrained soil: semi-analytical solution

**Hang Zhou*, Brian Sheil, Hanlong Liu**

**Prof. Hang Zhou (Corresponding author)**

Key Laboratory of New Technology for the Construction of Cities in Mountain Areas, College of Civil Engineering, Chongqing University, Chongqing, 400045, China

E-mail: zh4412517@163.com

**Dr. Brian Sheil**

Royal Academy of Engineering Research Fellow, Department of Engineering Science, University of Oxford, Parks Road, Oxford Ox1 3PJ, UK.

E-mail: brian.sheil@eng.ox.ac.uk

**Prof. Hanlong Liu**

Key Laboratory of New Technology for the Construction of Cities in Mountain Areas, College of Civil Engineering, Chongqing University, Chongqing, 400045, China

E-mail: cehliu@cqu.edu.cn

# Non-circular cavity expansion in undrained soil: semi-analytical solution

**Hang Zhou*, Brian Sheil, Hanlong Liu**

**ABSTRACT**

The cavity expansion approach has been a popular tool to interpret a wide range of geotechnical problems over the last several decades. Most previous research focused on the expansion of cylindrical and/or spherical cavities whereas ‘non-standard’ cavities have received much less attention. To address this shortcoming, this paper presents a general theoretical framework for two-dimensional (2D) displacement-controlled undrained non-circular cavity expansion (N-CCE) in undrained soil. The new approach combines strain path method (SPM) concepts and conformal mapping to determine the soil velocity and strain rate fields analytically. The soil displacement and strain are subsequently determined by integrating the soil velocities and strain rates along the strain path using a series of transformed ordinary differential equations. In this study, the modified Cam clay (MCC) effective stress constitutive model is used to determine the soil stress-strain relationship while consolidation effects are captured using finite difference calculations. The proposed methodology is validated by comparing the reduced solution for a circular cavity with traditional circular cavity expansion theory. A parametric analysis is subsequently undertaken to explore the influence of three non-circular cavity shapes on expansion-induced soil deformation mechanisms, shear strains, effective stresses, and pore water pressure development and consolidation. The proposed solution can be implemented with any critical state-based soil model and can be applied to arbitrary non-circular cavity problems.

**Keywords**: Non-circular cavity expansion; Undrained; Analytical solution; Strain; Excess pore pressure

## INTRODUCTION

Cavity expansion is a simple theoretical framework which has been used to interpret a wide range of geotechnical problems including displacement pile installation, pile end-bearing capacity, cone penetration testing and pressuremeter testing. A myriad of analytical and semi-analytical solutions have been developed using diverse solution techniques including the early closed-form approaches for an elastic-perfectly plastic medium (Gibson and Anderson 1961; Vesic 1972; Yu and Houlsby 1991; Mantaras and Schnaid 2002; Shuttle 2007), the similarity solution method (Collins and Stimpson 1994; Zhou et al., 2018a, 2021a) and Chen's method (Chen 2012, 2013, 2019) for critical state-based constitutive models. These published solutions have considered many complex soil behaviours including undrained/drained conditions (Collins and Stimpson 1994), soil dilatancy (Yu and Houlsby 1991), particle breakage (Liu et al., 2021), unsaturated effects (Chen et al., 2020), anisotropy (Li and Zou 2019), thermoplasticity (Zhou et al., 2018a), softening (Zhou et al., 2021b), viscoplasticity (Zhou et al., 2021c), and soil stratigraphy (Wang et al., 2019; Mo et al., 2017),.

Existing solutions are mainly limited to axisymmetric cavity problems. This limits application of the cavity expansion approach to 'non-standard' problems such as modeling the penetration behavior of X-section cast-in-place concrete ('XCC') piles (Liu et al., 2014; Sun et al., 2017; Zhou et al., 2017a, 2018b, 2019), rectangular piles (Basu & Salgado 2008; Seo et al., 2009) and prefabricated vertical drains (PVDs) mandrels (Ghandeharioon et al., 2010). For non-circular cavity expansion (N-CCE) in elastic media, theoretical solutions are feasible using complex variable elasticity (CVE) developed by Muskhelishvili (1954). Zhou et al. (2016, 2017b) explored the application of both displacement-controlled and pressure-controlled N-CCE to elastic soil and proposed a series of closed-form solutions using CVE. However, CVE is no longer suitable if soil plasticity is allowed to develop because the biharmonic stress function is often non-existent. Zhou et al. (2014) and Liu et al. (2016) proposed simplified solutions for N-CCE in elastic-perfectly plastic soil. Recently, Zhou et al. (2021d) proposed a semi-analytical solution for elliptical cavity expansion in a more realistic critical state-based modified Cam Clay (MCC) soil model. However, no general theoretical method exists for the expansion of arbitrary cavity shape. This gap motivates the present study, particularly for future applications to non-cylindrical pile performance.

The aim of this paper is to construct a general theoretical framework for two-dimensional displacement-controlled undrained N-CCE in undrained soil. This framework allows any critical state-based constitutive model to be incorporated; the widely adopted MCC model is adopted for this study. The proposed methodology is validated by comparing the reduced solution for a circular cavity with traditional circular cavity expansion theory. A parametric analysis explores the influence of three non-circular cavity shapes on expansion-induced soil deformation mechanisms, shear strains, effective stresses, and pore water pressure development and consolidation. The proposed solution can be implemented with any critical state-based soil model and can be applied to arbitrary non-circular cavity problems.

## PROBLEM DEFINITION AND BASIC ASSUMPTIONS

List of **Figure Captions**

Figure 1 defines the problem and notation for this study. A cavity with zero radius is expanded radially to an arbitrary non-circular cavity in an infinite soil domain. Cartesian coordinates $x$-$y$-$w$ and cylindrical coordinates system $r$-$\theta$-$w$ are used to describe the geometric features of N-CCE where $w$ defines the vertical coordinate to differentiate from the complex variable $z$ (= $x$+$iy$) where $i=\sqrt{-1}$ . Cavity expansion occurs in the $x$-$y$ or $r$-$\theta$ planes. For N-CCE, the radius of the non-circular boundary is nonconstant and defined as $R_c(\theta)$ where $\theta$ is the polar angle. The expansion velocity is $v_c$, which is equal to the derivative of the radius with respect to expansion time $t$. The initial total stress of the soil in the expansion ($x$-$y$, or $r$-$\theta$) plane is transversely isotropic (uniform) and defined as $\sigma_{h0}$ whereas $\sigma_{v0}$ is used to define the initial total stress in the $w$-direction. The initial pore pressure of the soil is $u_0$ such that the initial effective stress can be described as: $\sigma'_{h0}=\sigma_{h0}-u_0$ and $\sigma'_{v0}=\sigma_{v0}-u_0$. The critical state-based MCC model is used here to describe the stress-strain relationship of the soil. Three domains exist in the soil surrounding the cavity during expansion process: elastic, plastic (but pre critical state) and critical state domains.

The boundary of the non-circular cavity is assumed smooth (interface friction coefficient equals zero) thereby allowing the soil move tangentially to the boundary only. This is because the N-CCE soil deformations are derived using two-dimensional incompressible inviscid potential flow. Therefore, the soil and boundary velocities at the cavity-soil interface are not consistent and it is necessary to define the normal and tangential velocities of the soil at the interface, namely $v_n$ and $v_t$, where $v_n$ is equal to $v_c$ in the direction normal to the boundary surface.

## MATHEMATICAL FORMULATION: KINEMATICS

### *Governing equations for soil velocity*

The governing equation for soil velocity can be described by the following equations (derivations see Appendix A)

$$\frac{\partial^2\varphi}{\partial x^2}+\frac{\partial^2\varphi}{\partial y^2}=0 \tag{1}$$

$$v_x=\frac{\partial\varphi}{\partial x},\ v_y=\frac{\partial\varphi}{\partial y} \tag{2}$$

The velocity field for an incompressible medium is described by the Laplace equation which is solved using a new coordinate system, namely the 'conformal mapping coordinate system', for N-CCE.

### *Conformal mapping equation*

The conformal mapping technique is used to transform an arbitrary non-circular cavity to a unit circular cavity. As shown in Figure 2, the outer domain of the non-circular cavity in the $z$- (physical) plane is mapped into the outer domain of a unit circular cavity in the $\zeta$- (phase) plane. The N-CCE induced velocity boundary condition is also transformed from the $z$-plane to the $\zeta$- plane. The general conformal mapping equation for an arbitrary non-circular cavity is:

$$z(\zeta)=R\left(\zeta+\sum_{n=1}^{\infty}c_{2n-1}\zeta^{1-2n}\right) \qquad |\zeta|\geq 1 \tag{3}$$

where $R$ and $c_{2n-1}$ are conformal mapping parameters, which can be determined through the method of least squares (Zhou, 2017b) and $z=x+iy=re^{i\theta}$ and $\zeta=\xi+i\eta=\rho e^{i\omega}$. The parameters $R$ and $c_{2n-1}$ control the size and shape of the cavity, respectively. If $c_{2n-1}$=0, the cavity shape becomes a circle. If $n$=1 and $c_1$ is equal to a constant, the shape becomes an ellipse. If $n$ >1, the shape will become more complex. The term $c_{2n-1}\zeta^{1-2n}$ in Equation 3 means the cavity has a symmetric shape; if $c_n\zeta^n$ is instead used, the cavity becomes asymmetric. Figure 3 plots the conformal mapping coordinate system obtained from published classical solutions for circular, elliptical and square shapes and through iterative calculation using the method of least squares (Zhou, 2017b) for the X-shape.

***Transformation of the governing equations to the phase plane***

Equation (3) allows Equations (1) and (2) to be recast in the phase plane as follows (respectively):

$$\left|\frac{d\zeta}{dz}\right|^2\left(\frac{\partial^2\varphi}{\partial\xi^2}+\frac{\partial^2\varphi}{\partial\eta^2}\right)=0 \tag{4}$$

$$v_\xi=\frac{\partial\varphi}{\partial\xi},\quad v_\eta=\frac{\partial\varphi}{\partial\eta} \tag{5}$$

Since $|d\zeta/dz|^2$ is a nonzero positive number, Equation (4) becomes the well-known Laplace equation and can be expressed in a polar coordinate system as:

$$\frac{\partial^2\varphi}{\partial\rho^2}+\frac{1}{\rho}\frac{\partial\varphi}{\partial\rho}+\frac{1}{\rho^2}\frac{\partial^2\varphi}{\partial\omega^2}=0 \tag{6}$$

The general solution for Equation (6) is:

$$\varphi(\rho,\omega)=a_0+b_0\ln\rho+\sum_{n=1}^{\infty}\rho^{-n}(a_n\cos n\omega+b_n\sin n\omega) \tag{7}$$

where $a_0$, $b_0$, $a_n$ and $b_n$ are constant coefficients.

In addition, the radial and tangential velocity in the phase plane can be expressed as:

$$v_\rho=\frac{\partial\varphi}{\partial\rho},\ \ v_\omega=\frac{1}{\rho}\frac{\partial\varphi}{\partial\omega} \tag{8}$$

Combining Equations (7) and (8) yields the following expressions:

$$v_\rho=\frac{b_0}{\rho}+\sum_{k=1}^{\infty}\rho^{-k-1}(A_k\cos k\omega+B_k\sin k\omega) \tag{9}$$

$$v_\omega=\sum_{k=1}^{\infty}\rho^{-k-1}(A_k\sin k\omega-B_k\cos k\omega) \tag{10}$$

or:

$$(v_\rho+iv_\omega)=\frac{b_0}{\rho}+\sum_{k=1}^{\infty}\left(A_k-iB_k\right)\rho^{-k-1}e^{ik\omega} \tag{11}$$

where $A_k=-ka_k$, $B_k=-kb_k$ ($n$ =1, 2, 3…).

***Velocity boundary conditions***

We first define two unit vectors as follows:

$$\mathbf{e_n}=\mathbf{n}/|\mathbf{n}|=\left(\cos\lambda,\sin\lambda\right)\Leftrightarrow e^{i\lambda} \tag{12}$$

$$\mathbf{e_r}=\mathbf{r}/|\mathbf{r}|=\left(\cos\theta,\sin\theta\right)\Leftrightarrow e^{i\theta} \tag{13}$$

where $\mathbf{e_n}$ and $\mathbf{e_r}$ represent the unit vector in the cavity boundary normal and radial directions (respectively) in the physical plane (see Figure 4). Noting that

$$\mathrm{e}^{i\lambda}=\frac{dz}{|dz|}=\frac{z^{'}\left(\zeta\right)d\zeta}{\left|z^{'}\left(\zeta\right)\right|\left|d\zeta\right|}=\frac{\rho}{\overline{\zeta}}\frac{\left|z^{'}\left(\zeta\right)\right|}{\overline{z^{'}\left(\zeta\right)}} \tag{14}$$

$$e^{i\theta}=z\left(\zeta\right)/\left|z\left(\zeta\right)\right| \tag{15}$$

the cosine of the included angle between **n** and **r** at the cavity-soil boundary can be expressed as:

$$\cos(\mathbf{n},\mathbf{r})=\cos(\mathbf{e}_{\mathbf{n}},\mathbf{e}_{\mathbf{r}})=\mathbf{e}_{\mathbf{n}}\bullet\mathbf{e}_{\mathbf{r}}=\mathrm{Re}\left[\mathrm{e}^{i(\lambda-\theta)}\right]\Big|_{\zeta=\sigma} \tag{16}$$

where $\zeta|_{\rho=1}=\sigma=e^{i\omega}$ represents the cavity boundary.

The general expression for the radial distance in the $z$-plane from the non-circular cavity boundary to the origin center, $R_c(\theta)$, can be obtained from Equation (3):

$$R_c(\theta)\xrightarrow{\text{conformal mapping}}R_c(\omega)=|z(\zeta)|\big|_{\varsigma=\sigma}=|z(\sigma)| \tag{17}$$

where $|z(\sigma)|$ defines the modulus of $z$ at the cavity boundary.

The cavity boundary velocity can be expressed as:

$$v_c^{'}=\frac{dR_c(\theta)}{dt}=\frac{dR_c(\theta)}{dR}\frac{dR}{dt} \tag{18}$$

where $R$ is a kinematic parameter which is used here as a time scale proxy for convenience. The cavity boundary velocity can be re-defined as:

$$v_c=\frac{v_c^{'}}{dR/dt}=\frac{dR_c(\theta)}{dR} \tag{19}$$

Combining Equations (18) and (19) gives:

$$v_c=\frac{d|z(\sigma)|}{dR}=\frac{|z(\sigma)|}{R} \tag{20}$$

Given that the normal velocity components of the soil at the interface $v_n$ and the projected cavity boundary $v_c$ should be equal, one obtains:

$$v_n=v_c\cos(\mathbf{e}_{\mathbf{n}},\mathbf{e}_{\mathbf{r}})=\frac{1}{R}\left\{|z(\zeta)|\mathrm{Re}\left[\mathrm{e}^{i\lambda}|z(\zeta)|/z(\zeta)\right]\right\}_{\zeta=\sigma}=\frac{1}{R}\left\{\mathrm{Re}\left[\overline{z(\zeta)}\mathrm{e}^{i\lambda}\right]\right\}_{\zeta=\sigma} \tag{21}$$

Furthermore, the transformation between velocity components in the physical and phase planes can be expressed as (detailed derivation given in Appendix B):

$$v_x - iv_y = \frac{1}{z^{'}(\zeta)}(v_\xi - iv_\eta) = \frac{\mathrm{e}^{-i\omega}}{z^{'}(\zeta)}(v_\rho - iv_\omega) \tag{22}$$

According to the coordinate transformation relationship, one obtains:

$$v_x - iv_y\big|_{\zeta=\sigma} = e^{-i\lambda}\left(v_n - iv_t\right)\big|_{\zeta=\sigma} \tag{23}$$

Combining Equations (22) and (23) gives:

$$v_n - iv_t\big|_{\zeta=\sigma} = \left\{\frac{\left|z^{'}(\zeta)\right|}{\overline{z^{'}(\zeta)}}\frac{1}{z^{'}(\zeta)}\left(v_\rho - iv_\omega\right)\right\}_{\zeta=\sigma} = \left\{\frac{1}{\left|z^{'}(\zeta)\right|}\left(v_\rho - iv_\omega\right)\right\}_{\zeta=\sigma} \tag{24}$$

Thus, the velocity component $v_\rho\big|_{\zeta=\sigma}$ at the cavity boundary can be obtained as:

$$v_\rho\big|_{\zeta=\sigma} = \left\{v_n\left|z^{'}(\zeta)\right|\right\}_{\zeta=\sigma} = \frac{1}{R}\left\{\left|z^{'}(\zeta)\right|\mathrm{Re}\left[\overline{z(\zeta)}\mathrm{e}^{i\lambda}\right]\right\}_{\zeta=\sigma} = \frac{1}{R}\mathrm{Re}\left[\sigma z^{'}(\sigma)\overline{z(\sigma)}\right]V(\sigma) = V(\omega) \tag{25}$$

where the radial velocity in the phase plane is a function of the complex variable $\sigma$ (representing the cavity boundary) or the phase angle $\omega$.

***Closed-form expression for the field velocity***

Substituting the velocity boundary condition in Equation (25) into the general solution for $v_\rho$ ($\rho$=1) results in:

$$V(\omega) = b_0 + \sum_{k=1}^{\infty}(A_n \cos k\omega + B_n \sin k\omega) = \frac{A_0}{2} + \sum_{k=1}^{\infty}(A_k \cos k\omega + B_k \sin k\omega) \tag{26}$$

This is the standard form of Fourier series and the constant coefficients $A_k$ and $B_k$ can be evaluated through the following integrations:

$$A_k = \frac{1}{\pi}\int_{-\pi}^{\pi} V(\omega)\cos k\omega d\omega \quad \left(k = 0,1,2\cdots\infty\right) \tag{27}$$

$$B_k = \frac{1}{\pi}\int_{-\pi}^{\pi} V(\omega)\sin k\omega d\omega \quad \left(k = 1,2,3\cdots\infty\right) \tag{28}$$

Noting that $V(\omega)$ is an even function about $\omega$ and therefore $B_k = 0$, $A_k$ can be obtained by Equation (27) through numerical integration. Then, the final expression for the velocity in the $\zeta$- and $z$-planes can be obtained as (respectively):

$$(v_\rho + iv_\omega) = \frac{b_0}{\rho} + \sum_{k=1}^{\infty} A_k \rho^{-k-1} e^{ik\omega} \tag{29}$$

$$v_x + iv_y = \frac{\mathrm{e}^{i\omega}}{\overline{z^{'}(\zeta)}}(v_\rho + iv_\omega) = \frac{\mathrm{e}^{i\omega}}{\overline{z^{'}(\zeta)}}\left(\frac{b_0}{\rho} + \sum_{k=1}^{\infty} A_k \rho^{-k-1} e^{ik\omega}\right) \tag{30}$$

For convenience, Equation (30) is written with respect to the complex variables $\zeta$ and $\overline{\zeta}$ noting $\rho^2 = \zeta\overline{\zeta}$ and $\sigma^2 = \zeta / \overline{\zeta}$:

$$v_x + iv_y = \frac{1}{R\left[\overline{\zeta} + \sum_{n=1}^{\infty}(1-2n)c_{2n-1}\overline{\zeta}^{1-2n}\right]}\left(b_0 + \sum_{k=1}^{\infty} A_k \zeta^{-k}\right) = \frac{1}{\overline{\zeta}\,\overline{z^{'}(\zeta)}}\left(b_0 + \sum_{k=1}^{\infty} A_k \overline{\zeta}^{-k}\right) \tag{31}$$

***Closed-form expression for the strain rate***

Expressions for the strain rate components $\dot{\varepsilon}_x$, $\dot{\varepsilon}_y$, and $\dot{\varepsilon}_{xy}$ are obtained as the derivatives of the respective velocity components as follows:

$$\dot{\varepsilon}_x = -\frac{\partial v_x}{\partial x}, \quad \dot{\varepsilon}_y = -\frac{\partial v_y}{\partial y}, \quad \dot{\varepsilon}_{xy} = -\frac{1}{2}\left(\frac{\partial v_x}{\partial y} + \frac{\partial v_y}{\partial x}\right) \tag{32}$$

Then, we respectively define two new complex variables for velocity and strain rate as:

$$v_z = v_x + iv_y \tag{33}$$

$$\dot{\varepsilon}_z = \dot{\varepsilon}_x - \dot{\varepsilon}_y + 2i\dot{\varepsilon}_{xy} = -\frac{\partial v_z}{\partial x} - i\frac{\partial v_z}{\partial y} \tag{34}$$

Now, it is necessary to determine the derivative of $v_z$ with respect to *x* and *y* using the principle of multivariate function derivatives as follows:

$$\frac{\partial v_z}{\partial x} = \frac{\partial v_z}{\partial z}\frac{\partial z}{\partial x} + \frac{\partial v_z}{\partial \overline{z}}\frac{\partial \overline{z}}{\partial x} = \frac{\partial v_z}{\partial z} + \frac{\partial v_z}{\partial \overline{z}} \tag{35}$$

$$\frac{\partial v_z}{\partial y} = \frac{\partial v_z}{\partial z}\frac{\partial z}{\partial y} + \frac{\partial v_z}{\partial \overline{z}}\frac{\partial \overline{z}}{\partial y} = i\left(\frac{\partial v_z}{\partial z} - \frac{\partial v_z}{\partial \overline{z}}\right) \tag{36}$$

Subsequently, the complex variable strain rate can be transformed as:

$$\dot{\varepsilon}_z = -2\frac{\partial v_z}{\partial \overline{z}} \tag{37}$$

where $\overline{z}$ is the function of variable $\overline{\zeta}$ and thus,

$$\dot{\varepsilon}_z = -2\frac{\partial v_z}{\partial \overline{\zeta}}\frac{d\overline{\zeta}}{d\overline{z}} = -2\frac{\partial v_z}{\partial \overline{\zeta}}\frac{1}{\overline{z^{'}(\zeta)}} \tag{38}$$

It is more convenient to use the strain rate components in the mapping orthogonal curvilinear coordinate system in the $z$-plane for follow-on calculations of effective stress. The complex variable strain rate in the $\zeta$-plane can be defined as:

$$\dot{\varepsilon}_\zeta = \dot{\varepsilon}_\rho - \dot{\varepsilon}_\omega + 2i\dot{\varepsilon}_{\rho\omega} \tag{39}$$

where $\dot{\varepsilon}_\rho$, $\dot{\varepsilon}_\omega$, and $\dot{\varepsilon}_{\rho\omega}$ are the three strain components in the $\zeta$-plane.

The relationship between $\dot{\varepsilon}_\zeta$ and $\dot{\varepsilon}_z$ can be determined as (Muskhelishvili, 1954):

$$\dot{\varepsilon}_\zeta = \dot{\varepsilon}_z e^{-2i\lambda} = \dot{\varepsilon}_z \left\{ \frac{\overline{\zeta}}{\rho} \frac{\overline{z^{'}(\zeta)}}{\left|z^{'}(\zeta)\right|} \right\}^2 \tag{40}$$

The complex variable strain rate $\dot{\varepsilon}_\zeta$ can finally be obtained from Equations (38) and (3):

$$\dot{\varepsilon}_\zeta = -2\frac{\partial v_z}{\partial \overline{\zeta}}\frac{1}{\overline{z^{'}(\zeta)}}\left\{ \frac{\overline{\zeta}}{\rho} \frac{\overline{z^{'}(\zeta)}}{\left|z^{'}(\zeta)\right|} \right\}^2 = -2\frac{\partial v_z}{\partial \overline{\zeta}}\frac{\overline{\zeta}}{\zeta}\frac{1}{z^{'}(\zeta)} \tag{41}$$

where

$$\frac{\partial v_z}{\partial \overline{\zeta}} = -\frac{\left[\overline{z^{'}(\zeta)} + \overline{\zeta}\,\overline{z^{''}(\zeta)}\right]}{\left[\overline{\zeta}\,\overline{z^{'}(\zeta)}\right]^2}\left(b_0 + \sum_{k=1}^{\infty} A_k \overline{\zeta}^{-k}\right) + \frac{1}{\overline{\zeta}\,\overline{z^{'}(\zeta)}}\left(\sum_{k=1}^{\infty} -kA_k \overline{\zeta}^{-k-1}\right) \tag{42}$$

***Governing equations for displacement and strain in the phase plane***

The displacement and strain can be obtained by integrating the velocity and derivatives of the velocity, respectively:

$$dz = \int_0^R v_z\left(\zeta,\overline{\zeta},R\right)dR,\ \ d\overline{z} = \int_0^R \overline{v_z}\left(\zeta,\overline{\zeta},R\right)dR \tag{43}$$

$$d\varepsilon_\zeta = \int_0^R \dot{\varepsilon}_\zeta\left(\zeta,\overline{\zeta},R\right)dR,\ \ d\overline{\varepsilon_\zeta} = \int_0^R \overline{\dot{\varepsilon}_\zeta}\left(\zeta,\overline{\zeta},R\right)dR \tag{44}$$

The integration in Equations (43) and (44) is solved numerically since $\zeta$ and $\overline{\zeta}$ change during the cavity expansion process to consider large deformation effects. As the numerical integration is often intractable, these equations are transformed to ODEs by taking the derivatives of Equations (43) and (44) with respect to the kinematic parameter *R*:

$$\frac{dz}{dR} = v_z\left(\zeta,\overline{\zeta},R\right), \frac{d\overline{z}}{dR} = \overline{v_z}\left(\zeta,\overline{\zeta},R\right) \tag{45}$$

$$\frac{d\varepsilon_z}{dR} = \dot{\varepsilon}_z\left(\zeta,\overline{\zeta},R\right), \frac{d\overline{\varepsilon_z}}{dR} = \overline{\dot{\varepsilon}_z}\left(\zeta,\overline{\zeta},R\right) \tag{46}$$

The above equations can be considered an initial value problem (IVP), which can be solved using the Runge-Kutta method within an ODE solver. Furthermore, because the solutions are computed in the $\zeta$-plane, the complex variables $z$ and $\overline{z}$ should be transformed into the variables $\zeta$ and $\overline{\zeta}$. Considering $\frac{dz}{dR} = \frac{\partial z}{\partial R} + \frac{dz}{d\zeta}\frac{d\zeta}{dR}$ and $\frac{d\overline{z}}{dR} = \frac{\partial \overline{z}}{\partial R} + \frac{d\overline{z}}{d\overline{\zeta}}\frac{d\overline{\zeta}}{dR}$, Equations (45) and (46) become:

$$\frac{d\zeta}{dR} = \frac{d\zeta}{dz}\left[v_z\left(\zeta,\overline{\zeta},R\right) - \frac{z}{R}\right] = f_1\left(\zeta,\overline{\zeta},R\right) \tag{47}$$

$$\frac{d\overline{\zeta}}{dR} = \frac{d\overline{\zeta}}{d\overline{z}}\left[\overline{v_z}\left(\zeta,\overline{\zeta},R\right) - \frac{\overline{z}}{R}\right] = f_2\left(\zeta,\overline{\zeta},R\right) \tag{48}$$

$$\frac{d\varepsilon_\zeta}{dR} = \dot{\varepsilon}_\zeta\left(\zeta,\overline{\zeta},R\right) = f_3\left(\zeta,\overline{\zeta},R\right) \tag{49}$$

$$\frac{d\overline{\varepsilon_\zeta}}{dR} = \overline{\dot{\varepsilon}_\zeta}\left(\zeta,\overline{\zeta},R\right) = f_4\left(\zeta,\overline{\zeta},R\right) \tag{50}$$

Equations (47) to (50) can subsequently be condensed into matrix form as:

$$\frac{d\mathbf{K}}{dR} = \mathbf{F_k} \tag{51}$$

where $\mathbf{K} = \left[\zeta \quad \overline{\zeta} \quad \varepsilon_\zeta \quad \overline{\varepsilon_\zeta}\right]^T$, $\mathbf{F}_k = [f_1 \quad f_2 \quad f_3 \quad f_4]^T$. Equation (51) is the governing ODE for soil kinematics. To obtain the $z$-plane solution, the $\zeta$-plane variables $\zeta$ and $\overline{\zeta}$ can be mapped to the $z$-plane variables $Z$ and $\overline{z}$ using equation (3).

## MATHEMATICAL FORMULATION: EFFECTIVE STRESS

### *Constitutive model equations*

The effective stress can be computed by substituting the obtained strain state into a suitable constitutive model for the soil (MCC in this case). For MCC, the mean effective stress $p'$ and deviatoric stress $q$ can be written with respect to the stress components in a mapping coordinate system as:

$$p' = \frac{\sigma'_\rho + \sigma'_\omega + \sigma'_w}{3} \tag{52}$$

$$q = \frac{1}{\sqrt{2}}\sqrt{(\sigma'_\rho - \sigma'_\omega)^2 + (\sigma'_\omega - \sigma'_w)^2 + (\sigma'_w - \sigma'_\rho)^2 + 6\left(\tau^2_{\rho\omega} + \tau^2_{\omega w} + \tau^2_{w\rho}\right)} \tag{53}$$

For plane strain N-CCE, the shear stress components $\tau_{\omega w}$ and $\tau_{w\rho}$ are zero, and Equation (53) reduces to:

$$q = \frac{1}{\sqrt{2}}\sqrt{(\sigma'_\rho - \sigma'_\omega)^2 + (\sigma'_\omega - \sigma'_w)^2 + (\sigma'_w - \sigma'_\rho)^2 + 6\tau^2_{\rho\omega}} \tag{54}$$

The elastic-plastic constitutive relation for MCC model is (detailed derivations given in Appendix C):

$$\begin{bmatrix} \dfrac{d\varepsilon_\rho}{dR} \\ \dfrac{d\varepsilon_\omega}{dR} \\ \dfrac{d\varepsilon_w}{dR} \\ \dfrac{d\varepsilon_{\rho\omega}}{dR} \end{bmatrix} = \begin{bmatrix} C_{11} & C_{12} & C_{13} & C_{14} \\ C_{21} & C_{22} & C_{23} & C_{24} \\ C_{31} & C_{32} & C_{33} & C_{34} \\ C_{41} & C_{42} & C_{43} & C_{44} \end{bmatrix} \begin{bmatrix} \dfrac{d\sigma'_\rho}{dR} \\ \dfrac{d\sigma'_\omega}{dR} \\ \dfrac{d\sigma'_w}{dR} \\ \dfrac{d\tau_{\rho\omega}}{dR} \end{bmatrix} \tag{55}$$

where the expressions for the matrix elements are given in Appendix B.

For consistency, the strain components in Equation (55) should be written in complex variable form $\varepsilon_\zeta$

and $\overline{\varepsilon_\zeta}$. Since the constitutive relations contain four independent equations, two additional strains, namely the vertical strain $\varepsilon_w$ and the volumetric strain $\varepsilon_v$, are incorporated noting that both strains are zero (plane strain and incompressibility, respectively). Therefore, the constitutive equation (55) can be rewritten as:

$$\begin{bmatrix} \dfrac{d\varepsilon_\zeta}{dR} \\ \dfrac{d\overline{\varepsilon_\zeta}}{dR} \\ 0 \\ 0 \end{bmatrix} = \begin{bmatrix} C_{11}-C_{21}+2iC_{41} & C_{12}-C_{22}+2iC_{42} & C_{13}-C_{23}+2iC_{43} & C_{14}-C_{24}+2iC_{44} \\ C_{11}-C_{21}-2iC_{41} & C_{12}-C_{22}-2iC_{42} & C_{13}-C_{23}-2iC_{43} & C_{14}-C_{24}-2iC_{44} \\ C_{31} & C_{32} & C_{33} & C_{34} \\ C_{11}+C_{21} & C_{12}+C_{22} & C_{13}+C_{23} & C_{14}+C_{24} \end{bmatrix} \begin{bmatrix} \dfrac{d\sigma_\rho^{'}}{dR} \\ \dfrac{d\sigma_\omega^{'}}{dR} \\ \dfrac{d\sigma_w^{'}}{dR} \\ \dfrac{d\tau_{\rho\omega}}{dR} \end{bmatrix} \tag{56}$$

Equation (56) can be abbreviated as:

$$\frac{d\mathbf{E}}{dR} = \mathbf{C}\frac{d\mathbf{S}}{dR} \tag{57}$$

Defining $\mathbf{E}_R = d\mathbf{E}/dR$, $\mathbf{F}_s = \mathbf{C}^{-1}\mathbf{E}_R$ and rearranging Equation (57), the constitutive equations can be rewritten as the following uniform matrix:

$$\frac{d\mathbf{S}}{dR} = \mathbf{F}_s \tag{58}$$

Equation (58) is also a system of first-order ODEs and is coupled with Equation (51) through the soil position ($\zeta$, $\overline{\zeta}$).

## GOVERNING EQUATIONS FOR KINEMATICS AND EFFECTIVE STRESS

The solution for effective stress in Equation (58) requires input of the strain state. Thus the kinematics described by Equation (51) may be combined with the constitutive laws in Equation (58) to achieve a total governing equation:

$$\begin{bmatrix} \dfrac{d\mathbf{K}}{dR} \\ \dfrac{d\mathbf{S}}{dR} \end{bmatrix} = \begin{bmatrix} \mathbf{F}_k \\ \mathbf{F}_s \end{bmatrix} \tag{59}$$

which can be condensed further to:

$$\frac{d\mathbf{X}}{dR}=\mathbf{F} \tag{60}$$

The initial conditions are required to solve Equation (60): the initial soil position in the $\zeta$-plane is ($\zeta_0$, $\overline{\zeta_0}$) and the soil strain state is a zero vector. The initial condition for **X**, **K** and **S** can therefore be defined as:

$$\mathbf{X_0}=\left[\mathbf{K_0} \quad \mathbf{S_0}\right]^T \tag{61}$$

$$\mathbf{K}_0=\left[\zeta_0 \quad \overline{\zeta_0} \quad 0 \quad 0\right]^T \tag{62}$$

$$\mathbf{S_0}=\left[\sigma'_{\rho 0} \quad \sigma'_{\omega 0} \quad \sigma'_{\mathrm{w}0} \quad \tau_{\rho\omega,0}\right]^T \tag{63}$$

where the subscript '0' indicates the initial condition for the corresponding variable or vector and $\left[\sigma'_{\rho 0} \quad \sigma'_{\omega 0} \quad \sigma'_{\mathrm{w}0} \quad \tau_{\rho\omega,0}\right]=\left[\sigma'_{\mathrm{h}0} \quad \sigma'_{\mathrm{h}0} \quad \sigma'_{v0} \quad 0\right]$. The transformations between strain and effective stress in the $z$- and $\zeta$-planes are provided in Appendix D.

# MATHEMATICAL FORMULATION: PORE WATER PRESSURE

## *Stress equilibrium equations in orthogonal curvilinear coordinates*

Considering only force balance in the expansion (horizontal) plane for plane strain conditions, the stress equilibrium equations in orthogonal curvilinear coordinates can be expressed as:

$$\frac{\partial\sigma_\rho}{\partial\rho}+\frac{1}{\rho}\frac{\partial\tau_{\rho\omega}}{\partial\omega}+\left(1+\rho\frac{H_\rho}{H}\right)\frac{\left(\sigma_\rho-\sigma_\omega\right)}{\rho}+2\frac{H_\omega}{H}\frac{\tau_{\rho\omega}}{\rho}=0 \tag{64}$$

$$\frac{1}{\rho}\frac{\partial\sigma_\omega}{\partial\omega}+\frac{\partial\tau_{\rho\omega}}{\partial\rho}-\frac{H_\omega}{H}\frac{\left(\sigma_\rho-\sigma_\omega\right)}{\rho}+2\left(1+\rho\frac{H_\rho}{H}\right)\frac{\tau_{\rho\omega}}{\rho}=0 \tag{65}$$

Where

$$H_\rho=\frac{\partial H}{\partial\rho}=\frac{1}{R}\mathrm{Re}\left[z''(\zeta)\sqrt{\overline{z'(\zeta)}/z'(\zeta)}\right] \tag{66}$$

$$H_\omega=\frac{\partial H}{\partial\omega}=\frac{1}{R}\mathrm{Re}\left[i\rho\sigma z''(\zeta)\sqrt{\overline{z'(\zeta)}/z'(\zeta)}\right] \tag{67}$$

$z'$ and $z''$ are the first and second derivatives of the conformal mapping function with respect to $\zeta$. Incorporating the effective stress principle, Equations (64) and (65) can be expressed as:

$$\frac{\partial u}{\partial \rho}+\frac{\partial \sigma_{\rho}^{'}}{\partial \rho}+\frac{1}{\rho}\frac{\partial \tau_{\rho\omega}}{\partial \omega}+\left(1+\rho\frac{H_{\rho}}{H}\right)\frac{\left(\sigma_{\rho}^{'}-\sigma_{\omega}^{'}\right)}{\rho}+2\frac{H_{\omega}}{H}\frac{\tau_{\rho\omega}}{\rho}=0 \tag{68}$$

$$\frac{1}{\rho}\frac{\partial u}{\partial \omega}+\frac{1}{\rho}\frac{\partial \sigma_{\omega}^{'}}{\partial \omega}+\frac{\partial \tau_{\rho\omega}}{\partial \rho}-\frac{H_{\omega}}{H}\frac{\left(\sigma_{\rho}^{'}-\sigma_{\omega}^{'}\right)}{\rho}+2\left(1+\rho\frac{H_{\rho}}{H}\right)\frac{\tau_{\rho\omega}}{\rho}=0 \tag{69}$$

***Numerical integration solution along $\rho$ direction***

Closed-form analytical solutions for Equations (68) and (69) are not guaranteed and therefore they are computed using numerical integration. The stress equilibrium equation (68) along the $\rho$ direction is selected for integration as:

$$u\left(\rho,\ \omega\right)=u_{0}+\int_{\rho}^{\infty}\left[\frac{\partial \sigma_{\rho}^{'}}{\partial \rho}+\frac{1}{\rho}\frac{\partial \tau_{\rho\omega}}{\partial \omega}+\left(1+\rho\frac{H_{\rho}}{H}\right)\frac{\left(\sigma_{\rho}^{'}-\sigma_{\omega}^{'}\right)}{\rho}+2\frac{H_{\omega}}{H}\frac{\tau_{\rho\omega}}{\rho}\right]d\rho \tag{70}$$

## MATHEMATICAL FORMULATION: SUBSEQUENT CONSOLIDATION

To account for post-expansion consolidation, Terzaghi's two-dimensional consolidation theory is adopted. The pore pressure *u* can be expressed as:

$$\frac{\partial u}{\partial t}=c_{v}\nabla^{2}u \tag{71}$$

where $c_v$ is the coefficient of consolidation. When transformed to the $\zeta$-plane, Equation (71) becomes:

$$\frac{\partial u}{\partial t}=c_{v}\left|\frac{d\zeta}{dz}\right|^{2}\left(\frac{\partial^{2}u}{\partial \rho^{2}}+\frac{1}{\rho}\frac{\partial u}{\partial \rho}+\frac{1}{\rho^{2}}\frac{\partial^{2}u}{\partial \omega^{2}}\right) \tag{72}$$

The Crank-Nicolson finite difference method (FDM) is adopted to obtain the numerical solution of Equation (72). Applying the Crank–Nicolson discretization and letting $u\left(i\Delta\rho,\ j\Delta\omega,\ n\Delta t\right)=u_{i,\mathrm{j}}^{n}$, $\left|d\zeta/dz\right|^{2}=f_{i,j}$, Equation (72) can be transformed as follows:

$$\begin{aligned}&\left(1+2\lambda_{\rho}+2\lambda_{\omega}\right)u_{i,j}^{n+1}-\left(\lambda_{\rho}+\alpha\right)u_{i-1,j}^{n+1}-\left(\lambda_{\rho}-\alpha\right)u_{i+1,j}^{n+1}-\lambda_{\omega}u_{i,j+1}^{n+1}-\lambda_{\omega}u_{i,j-1}^{n+1}\\&=\left(\lambda_{\rho}+\alpha\right)u_{i-1,j}^{n}+\left(1-2\lambda_{\rho}-2\lambda_{\omega}\right)u_{i,j}^{n}+\left(\lambda_{\rho}-\alpha\right)u_{i+1,j}^{n}+\lambda_{\omega}u_{i,j+1}^{n}+\lambda_{\omega}u_{i,j-1}^{n}\end{aligned} \tag{73}$$

where $u_{i,\mathrm{j}}^{n}$ defines the pore pressure at node (*i*, *j*) at step *n* and $f_{i,j}$ is independent of time *t*. In addition, $\lambda_{\rho}=\left(c_{v}\Delta t/2\Delta\rho^{2}\right)f_{i,j}$, $\lambda_{\omega}=\left(c_{v}\Delta t/2\rho^{2}\Delta\omega^{2}\right)f_{i,j}$, $\alpha=-\left(c_{v}\Delta t\right)/\left(4\rho\Delta\rho\right)$.

The boundary conditions and finite difference grids in the $\zeta$-plane are shown in Figure 5. The cavity-soil interface is treated as impermeable ($\partial u/\partial\rho=0$). An artificial outer boundary of the computational domain with $\rho=\rho_b$ is prescribed the initial ('free-field') pore pressure $u_0$; to avoid boundary effects $\rho_b$ is selected as 50 times the maximum radius of the elastic-plastic boundary in the $\zeta$-plane. Given the symmetry of the cavity shapes considered (see Figure 3), only a quarter of the model from $\omega=0$ to $\omega=\pi/2$ is analysed and the pore pressure gradient tangential to the symmetry boundaries is zero. Subsequently, Equation (73) can be solved using the iterative successive over-relaxation (SOR) algorithm as follows:

$$u_{i,j}^{n+1}=\frac{1}{\left(1+2\lambda_\rho+2\lambda_\omega\right)}\left(G_{i,j}^{n+1}+G_{i,j}^{n}\right) \tag{74}$$

$$G_{i,j}^{n+1}=\left(\lambda_\rho+\alpha\right)u_{i-1,j}^{n+1}+\left(\lambda_\rho-\alpha\right)u_{i+1,j}^{n+1}+\lambda_\omega u_{i,j+1}^{n+1}+\lambda_\omega u_{i,j-1}^{n+1} \tag{75}$$

$$G_{i,j}^{n}=\left(\lambda_\rho+\alpha\right)u_{i-1,j}^{n}+\left(\lambda_\rho-\alpha\right)u_{i+1,j}^{n}+\lambda_\omega u_{i,j+1}^{n}+\lambda_\omega u_{i,j-1}^{n} \tag{76}$$

where $G_{i,j}^{n}$ $(n=1)$ is already known and represents the initial excess pore pressure distribution. The initial value of $G_{i,j}^{n+1}$ $(n=1)$ is unknown but can be assumed as $G_{i,j}^{n}$ $(n=1)$ to start the iteration. Then, two additional parameters $u_{i,j}^{n+1}\big|_{old}$ and $u_{i,j}^{n+1}\big|_{new}$ are defined to represent the old and new calculated values of pore pressure (respectively). Substituting the two parameters and updating the expression of Equation (75):

$$G_{i,j}^{n+1}=\left(\lambda_\rho+\alpha\right)u_{i-1,j}^{n+1}\big|_{new}+\left(\lambda_\rho-\alpha\right)u_{i+1,j}^{n+1}\big|_{old}+\lambda_\omega u_{i,j+1}^{n+1}\big|_{old}+\lambda_\omega u_{i,j-1}^{n+1}\big|_{new} \tag{77}$$

Then, the final expression for FDM calculation can be obtained as:

$$u_{i,j}^{n+1}\big|_{new}=\left(1-\varpi_0\right)u_{i,j}^{n+1}\big|_{old}+\frac{1}{\left(1+2\lambda_\rho+2\lambda_\omega\right)}\left(G_{i,j}^{n+1}+G_{i,j}^{n}\right)\varpi_0 \tag{78}$$

where $0<\varpi_0<2$ is a SOR factor. Setting an error tolerance ER for the iteration as:

$$\mathrm{ER}=\frac{\left|u_{i,j}^{n+1}\big|_{new}-u_{i,j}^{n+1}\big|_{old}\right|}{u_{i,j}^{n+1}\big|_{new}}\leq 10^{-5} \tag{79}$$

Equation (79) is repeatedly computed until ER $\leqslant 10^{-5}$.

## VALIDATION

### *Comparison of reduced CCE solutions with published solutions*

To validate the proposed methodology, calculations for the expansion of a circular cavity are compared with those determined using traditional CCE solutions. For undrained CCE, the kinematics including radial displacement, three strain components in polar coordinates system can be written as:

$$\frac{u_r}{R} = \frac{r}{R} - \sqrt{\left(\frac{r}{R}\right)^2 - 1} \tag{80}$$

$$\varepsilon_r = -\frac{1}{2}\ln\left[1 - \left(\frac{R}{r}\right)^2\right],\ \varepsilon_\theta = \frac{1}{2}\ln\left[1 - \left(\frac{R}{r}\right)^2\right],\ \varepsilon_{r\theta} = 0 \tag{81}$$

where $u_r$ is the radial displacement of the soil and, in this case, the kinematic parameter $R$ reduces to the radius of the cylindrical cavity after expansion; $\varepsilon_r, \varepsilon_\theta, \varepsilon_{r\theta}$ are the three strain components in polar coordinates. For the calculation of the effective stress and excess pore pressure, the rigorous semi-analytical solution proposed by Chen & Absouleiman (2012) is used here for comparison. Figure 6 compares calculations of the development of normalized radial displacement, $u_r/R$, and three polar strain components with normalized radial distance, $r/R$, using the proposed approach and the solutions of Chen & Absouleiman (2012). Similarly, calculations of the development of radial excess pore pressure at the cavity boundary, $\Delta u_a$ (normalized by the undrained shear strength $s_u$) with normalized radial expansion, $R/R_0$, are compared in Figure 7 where $R_0$ is the radius of the initial cylindrical cavity prior to expansion. In Figure 7, three different isotropic overconsolidation ratios, $R_{oc}$, are considered where $R_{oc}= p_c^{'} / p_0^{'}$. Finally, calculations of the variation of the three cartesian effective stresses, normalized by $s_u$, with normalized radial distance is presented in Figures 8a ($R_{oc}$ = 1) and 8b ($R_{oc}$ = 10). In all cases, calculations using the present solutions are in exact agreement with those determined using the CCE solution proposed by Chen & Absouleiman (2012).

In addition, present calculations of pore water pressure dissipation are compared to those determined using the approach of Randolph & Wroth (1979) as a function of normalized radial distance ($r/R$) and normalized time ($c_v t/R^2$) in Figure 9a and 9b respectively. For the sake of comparison, the initial excess pore pressure is also generated using the Randolph & Wroth (1979) solutions: $\Delta u/s_u = 2\ln\left(r_p/r\right)$, where $r_p$ is the radius of the plastic zone defined as $r_p/R = \sqrt{G/s_u}$ . The comparisons in Figure 9 show that present consolidations calculations are in excellent agreement with the Randolph & Wroth (1979) closed-form solutions.

## RESULTS: N-CCE DEFORMATION MECHANISMS

### *Soil velocity vectors and displacement*

Figure 10 plots the soil velocity vector field caused by the expansion of a circular (Fig. 10(a)), elliptical (Fig. 10(b)), square (Fig. 10(c)) and X-shaped (Fig. 10(d)) cavity. Only the upper right-hand quadrant of the model is presented due to symmetry. For the non-circular cavities, the radial distance is normalized by the dimension of the major axis ($R_{\mathrm{cmax}}$). For the circular cavity, soil velocity vectors are orientated in the radial direction only, which is consistent with traditional CCE theory. For the elliptical cavity, the deformation pattern is no longer symmetrical and expansion causes both radial and tangential soil velocities in the vicinity surrounding the cavity. The soil particle velocities at the cavity-soil interface act in a direction normal to the surface of the ellipse; the subsequent trajectory with increasing radial distance coincides with the $\rho$ direction of the conformal mapping coordinate system (Fig. 3). For the square and X-shaped cavities, the soil velocity trajectories exhibit more complex modes and do not coincide with the direction of $\rho$. In particular, both normal and tangential velocities now occur at the cavity-soil interface, with the exception of the symmetry axis where the tangential velocity is zero.

Interestingly, the N-CCE velocity fields tend towards an equivalent CCE field as the radial distance from the cavity increases. This indicates that the influence of the cavity shape is limited to a certain zone of soil surrounding the cavity. Figure 11 compares the distribution of expansion-induced normalized radial displacements, $u_r/ R_c(\theta)$, for CCE ($\theta$ = any) with N-CCE along different axes of symmetry: $\theta = 0$ and $\pi/2$ (elliptical), $\theta = 0$ and $\pi/4$ (square and X-shaped). It is found that the distribution of normalized radial displacement is highly dependent on the adopted radial direction $\theta$. Results for the elliptical cavity are most sensitive to $\theta$ and provide both an upper ($\theta = \pi/2$; minor axis) and lower ($\theta = 0$; major axis) bound to all results, followed by the X-shaped and square cavities.

***Maximum shear strain***

For plane strain N-CCE, the maximum shear strain is obtained from the cartesian strain components as follows:

$$\gamma_{\max} = \tfrac{\sqrt{2}}{3}\sqrt{(\varepsilon_x - \varepsilon_y)^2 + \varepsilon_x^2 + \varepsilon_y^2 + 6\varepsilon_{xy}^2} \tag{82}$$

Figure 12 shows contours of maximum shear strain, $\gamma_{max}$, caused by the expansion of the four different cavity shapes. The circular cavity results are perfectly axisymmetric, which is again consistent with traditional CCE (Fig. 12(a)). As expected, this axisymmetry is not applicable to the non-circular cavities. For an elliptical cavity, the $\gamma_{max}$ contours near the cavity also resemble an elliptical shape, with the maximum value of $\gamma_{max}$ occurring at the cavity-soil interface at $\theta = 0$ (see Fig. 12(b)). However, the geometric similarity between cavity shape and the $\gamma_{max}$ contours gradually disappears with increasing radial distance. For square and X-shaped cavity expansion, strain concentrations occur at the cavity corners (Figs. 12(c) and 12(d) respectively). Near the cavity-soil interface, the $\gamma_{max}$ contours resemble a 'smoothened' version of the cavity shape which then transition towards a circular shape when the radial distance becomes sufficiently large.

## RESULTS: N-CCE SOIL STRESS CHANGES

### *Shear stress distribution immediately post cavity expansion*

The kinematics of the cavity expansion problem are independent of the soil model. For calculation of soil stresses and pore water pressures, parameters for Boston Blue clay (BBC) a were selected. The soil properties can be summarized as: $\lambda = 0.15$, $\kappa = 0.03$, $M = 1.2$, $\nu' = 0.278$, $\upsilon_{cs} = 2.74$, $K_0 = 2$, $\sigma'_{r0} = \sigma'_{\theta 0} = 144$ kPa, $\sigma'_{z0} = 72$ kPa, $u_0 = 100$ kPa, OCR=10 (Chen and Absouleiman (2012)). Note that OCR=$\sigma'_{zc}/\sigma'_{z0}$, which is different from $R_{oc}$= $p'_c/p'_0$. Contours of normalized shear stress $\tau_{r\theta}/s_u$ immediately post cavity expansion are presented in Figure 13. Due to axisymmetry, traditional CCE does not cause shear stress development unlike the N-CCE calculations (see Figure 13(a)). As shown in Figure 13(b), contours of shear stress induced by elliptical cavity expansion form 'stress bubbles' emanating from the cavity-soil interface. The shear stress reaches a maximum value at the lower left-hand portion ($0 < \theta < \pi/4$) of the interface and subsequently vanishes towards $\theta = 0$ and $\theta = \pi/2$ (owing to the axes of symmetry). For square cavity expansion, the shear stress contours are now 'heart-shaped' and are symmetric about $\theta = \pi/4$ (see Figure 13(c)). In this case, the maximum shear stress occurs at the corner of the square cavity-soil interface ($\theta = \pi/4$), where a stress concentration occurs. These findings are equally applicable to the 'butterfly-shaped' contours for the X-shaped cavity in Figure 13(d) which also show stress concentrations at the cavity corners with one notable exception: the stress concentrations are notably smaller in size for the X-shaped cavity compared to a square cavity.

### *Effective stress distribution immediately post cavity expansion*

Figure 14 compares the distribution of normalized radial, tangential and vertical effective soil stress ($\sigma_r'/s_u$, $\sigma_\theta'/s_u$ and $\sigma_w'/s_u$, respectively) for CCE ($\theta$ = any) with N-CCE along different axes of symmetry: $\theta = 0$ and $\pi/2$ (elliptical), $\theta = 0$ and $\pi/4$ (square and X-shaped). It can be found that the cavity shape has a notable influence on the radial distribution of effective stress. The effective soil stresses near the cavity boundary are independent of the cavity shape because undrained soil conditions have been achieved. Immediately outside the critical state zone, the soil is in a plastic state where the three normalized effective stress components show slight dependence on cavity shape due to the different levels of strain caused by the cavity expansion. When the distance to the cavity center is sufficiently large, the soil is in an elastic state and the effective stress is consistent across all shapes.

The variation of normalized radial, tangential, vertical effective stress and shear stress with $\theta$ at the cavity-soil interface is explored in Figure 15. For a circular cavity, the effective stress state at the cavity-soil interface is independent of $\theta$ (Figure 15(a)). In contrast, the four effective stress components are highly sensitive to $\theta$ for N-CCE. For an elliptical cavity, the variation in the stress state with $\theta$ is smooth with local optima occurring for all four stress components at $\theta \approx 0.14\pi$ except for $\tau_{r\theta}$ which occurs at $\theta \approx 0.06\pi$ (Figure 15(b)). These local minima depend on the shear stress distribution, which is related to the elliptic curvature of the cavity. An elliptical aspect ratio of $\beta = 2$ is considered in this study; the position of local optima will be different for alternative values of $\beta$. For a square cavity, $\theta = \pi/4$ is a symmetry axis such that the results are mirrored (Figure 15(c)). These results show a more complex dependence on $\theta$ with notable stress concentrations occurring at the corners ($\theta = \pi/4$). The tangential stress component, $\sigma'_\theta$, is most affected by a change in $\theta$, followed by $\sigma'_r$. In contrast, $\sigma'_w$ experiences little change. These findings are equally applicable to the X-shaped cavity results in Figure 15(d) though the trends are slightly more complex. For example, in the region $0.1\pi \leqslant \theta \leqslant 0.4\pi$ (concave arc segment of X-shaped cavity) the distribution of $\sigma'_r$ resembles a 'W' shape, the distributions of $\sigma'_\theta$ and $\sigma'_w$ are similar to a 'U' shape, while the distribution of the $\tau_{r\theta}$ is a 'V' shape.

***Excess pore pressure distribution immediately after cavity expansion***

Figure 16 plots contours of normalized excess pore pressure, $\Delta u/s_u$, immediately post cavity expansion for all four cavity shapes. Unlike the axisymmetric pore pressure field for CCE, the N-CCE results are more complex. In particular, a concentration in $\Delta u$ occurs towards the cavity corners for the square and X-shaped cavities similar to what was observed for the shear stresses in Figure 13. As the radial distance from the cavity is increased, these distributions again revert towards circular distributions. Negative excess pore pressure also develops in the soil owing to the large OCR for BBC (OCR=10).

***Post-expansion consolidation***

Figure 17 shows the radial distribution (along symmetry axis) of the normalized excess pore pressure surrounding the cavity at four different stages of consolidation. At the cavity-soil interface, the excess pore pressures are positive for all cavity shapes except for the X-shaped cavity along a path of $\theta = \pi/4$. These excess pore pressures gradually subside as consolidation progresses. It can also be seen that the radial distribution of $\Delta u$ is sensitive to both the cavity shape and the adopted value of $\theta$.

Figure 18 plots the variation of $\Delta u$ along the cavity-soil interface for all four cavities and considering the same four stages of consolidation. For CCE, the excess pore pressures at the cavity-soil interface are independent of θ and reduce uniformly during consolidation (Figure 18(a)). Interestingly, for an elliptical cavity the maximum excess pore pressure occurs at $\theta = 0$ only once consolidation has commenced (Figure 18(b)). As consolidation progresses, the distribution of $\Delta u$ with $\theta$ becomes more uniform. This 'homogenization' of excess pore pressures during consolidation is also observed for the square and X-shaped cavities in Figure 18(c) and Figure 18(d), respectively. The initial excess pore pressure immediately after expansion for a square cavity expansion resembles an inverted V-shape, while the one at the concave arc segment for X-shaped cavity expansion is similar to an 'M' shape. Finally, negative excess pore pressures occur near the corner of X-shaped cavity, which were not immediately apparent from previous contours of $\Delta u$.

**CONCLUSIONS**

In this paper, a general theoretical framework is proposed for undrained non-circular cavity expansion (N-CCE) in soil obeying undrained soil mechanics. Closed-form solutions for the soil velocity and strain rate of N-CCE were derived by combining strain path method concepts with conformal mapping. Semi-analytical solution for the soil displacement, strain and effective stress were obtained by solving a system of ordinary differential equations using the Runge-Kutta method. The cavity expansion induced excess pore pressure is calculated by solving the stress equilibrium equation through numerical integration and the subsequent consolidation process is captured by solving the consolidation equation using finite difference calculations.

A parametric analysis was undertaken to explore the influence of three different non-circular cavities including ellipse, square and X-shaped. Distributions of soil displacement, strain, effective stress and excess pore pressure were presented with a focus on differences between present analytical predictions and conventional cylindrical cavity expansion theory. The results showed that soil velocities for elliptical cavity expansion coincide with the $\rho$ direction of the conformal mapping coordinate system, unlike square and X-shaped cavities which show more complex modes. For non-circular sections, the distribution of normalized radial displacement was shown to be highly dependent on the adopted radial direction $\theta$. In addition, shear stress contours for elliptical revealed the presence of 'stress bubbles' whereas 'heart-shaped' and 'butterfly-shaped' stress concentrations were observed for the square and X-shaped cavities respectively. Finally, the initially highly non-uniform excess pore pressures surrounding the cavity-soil interface gradually tend a uniform distribution (circumferentially) as consolidation progresses.

The proposed semi-analytical solution can be implemented with any critical state-based soil model and can be applied to arbitrary non-circular cavity problems. It has significant potential for application to noncylindrical penetrators, (to evaluate the 'smear' effect for vertical drain installation and the installation effect of XCC pile), and flat dilatometers tests (interpretation of testing data).

## APPENDIX A：GOVERNING EQUATION FOR SOIL VELOCITY

This paper focuses on cohesive soils such that the initial cavity expansion phase is undrained; volumetric strains and strain rates are therefore assumed zero during expansion of the cavity. The volumetric strain rate, $\dot{\varepsilon}_v$, can be written as the sum of the three strain rate components in the Cartesian coordinate system ($\dot{\varepsilon}_x$, $\dot{\varepsilon}_y$ and $\dot{\varepsilon}_w$) as:

$$\dot{\varepsilon}_v = \dot{\varepsilon}_x + \dot{\varepsilon}_y + \dot{\varepsilon}_w = 0 \tag{A1}$$

Since cavity expansion only occurs in the *x-y* plane and $\dot{\varepsilon}_w = 0$ for plane strain conditions, Equation (A1) reduces to:

$$\dot{\varepsilon}_x + \dot{\varepsilon}_y = 0 \tag{A2}$$

Incorporating the velocity-strain rate relationship, Equation (A2) becomes:

$$\frac{\partial v_x}{\partial x} + \frac{\partial v_y}{\partial y} = 0 \tag{A3}$$

where $v_x$ and $v_y$ are the two velocity components in the Cartesian coordinate system.

The SPM (Baligh, 1985) assumption that soil movement is nonrotational is also adopted here:

$$\frac{\partial v_y}{\partial x} - \frac{\partial v_x}{\partial y} = 0 \tag{A4}$$

Equations (A4) are the well-known Cauchy-Riemann equations, which require a potential function $\varphi$ to satisfy the following relationships:

$$v_x = \frac{\partial \varphi}{\partial x} \tag{A5}$$

$$v_y = \frac{\partial \varphi}{\partial y} \tag{A6}$$

Substituting Equations (A5) and (A6) into Equation (A3) leads to:

$$\frac{\partial^2 \varphi}{\partial x^2} + \frac{\partial^2 \varphi}{\partial y^2} = 0 \tag{A7}$$

## APPENDIX B: TRANSFORMATION OF VELOCITY FROM PHASE PLANE TO PHYSICAL PLANE

The transformation between physical and phase plane velocities can be derived as:

$$\begin{aligned} v_x - i v_y &= \frac{\partial \varphi}{\partial x} - i\frac{\partial \varphi}{\partial y} = \left(\frac{\partial \varphi}{\partial \xi}\frac{\partial \xi}{\partial x} + \frac{\partial \varphi}{\partial \eta}\frac{\partial \eta}{\partial x}\right) - i\left(\frac{\partial \varphi}{\partial \xi}\frac{\partial \xi}{\partial y} + \frac{\partial \varphi}{\partial \eta}\frac{\partial \eta}{\partial y}\right) \\ &= \left(\frac{\partial \xi}{\partial x} - i\frac{\partial \xi}{\partial y}\right)\frac{\partial \varphi}{\partial \xi} + \left(\frac{\partial \eta}{\partial x} - i\frac{\partial \eta}{\partial y}\right)\frac{\partial \varphi}{\partial \eta} = 2\frac{\partial \xi}{\partial z}\frac{\partial \varphi}{\partial \xi} + 2\frac{\partial \eta}{\partial z}\frac{\partial \varphi}{\partial \eta} \\ &= \left(2\frac{\partial \xi}{\partial \zeta}\frac{\partial \varphi}{\partial \xi} + 2\frac{\partial \eta}{\partial \zeta}\frac{\partial \varphi}{\partial \eta}\right)\frac{d\zeta}{dz} = (v_\xi - i v_\eta)\frac{1}{z'(\zeta)} \end{aligned} \tag{B1}$$

In addition, the following relationship is obtained:

$$(v_\xi - i v_\eta) = (v_\rho - i v_\omega)\mathrm{e}^{-i\omega} \tag{B2}$$

$$(v_x - i v_y) = (v_r - i v_\theta)\mathrm{e}^{-i\theta} \tag{B3}$$

## APPENDIX C: ELASTIC-PLASTIC CONSTITUTIVE RELATION

The yield function in the MCC model can be expressed as (Wood, 1990):

$$F\left(p', q, p_c\right) = q^2 - M^2\left[p'\left(p_c' - p'\right)\right] \tag{C1}$$

where $p_c'$ is the hardening parameter describing the preconsolidation pressure under isotropic compression.

The incremental plastic strain component assuming associated plastic flow is:

$$d\varepsilon_\rho^p = \Lambda\left[\frac{p'\left(M^2 - \eta^2\right)}{3} + 3\left(\sigma'_\rho - p'\right)\right] \tag{C2}$$

$$d\varepsilon_\omega^p = \Lambda\left[\frac{p'\left(M^2 - \eta^2\right)}{3} + 3\left(\sigma'_\omega - p'\right)\right] \tag{C3}$$

$$d\varepsilon_w^p = \Lambda\left[\frac{p'\left(M^2 - \eta^2\right)}{3} + 3\left(\sigma'_w - p'\right)\right] \tag{C4}$$

$$d\varepsilon_{\rho\omega}^p = \Lambda\left(3\tau_{\rho\omega}\right) \tag{C5}$$

where $\Lambda = \frac{\lambda - \kappa}{\upsilon p^{'2}\left(M^2+\eta^2\right)}\left(dp^{'} + \frac{2\eta}{M^2-\eta^2}dq\right)$, $\eta = \frac{q}{p^{'}}$.

Equations (C2)-(C5) can be summarized in matrix form as:

$$\begin{bmatrix} \frac{d\varepsilon_\rho^p}{dR} \\ \frac{d\varepsilon_\omega^p}{dR} \\ \frac{d\varepsilon_w^p}{dR} \\ \frac{d\varepsilon_{\rho\omega}^p}{dR} \end{bmatrix} = \varpi \begin{bmatrix} a_\rho^2 & a_\rho a_y & a_\rho a_z & a_\rho a_{\rho\omega} \\ a_\omega a_\rho & a_\omega^2 & a_\omega a_z & a_\omega a_{\rho\omega} \\ a_z a_\rho & a_z a_\omega & a_z^2 & a_z a_{\rho\omega} \\ a_{\rho\omega} a_\rho & a_{\rho\omega} a_\omega & a_{\rho\omega} a_z & a_{\rho\omega}^2 \end{bmatrix} \begin{bmatrix} \frac{d\sigma_\rho^{'}}{dR} \\ \frac{d\sigma_\omega^{'}}{dR} \\ \frac{d\sigma_w^{'}}{dR} \\ \frac{d\tau_{\rho\omega}}{dR} \end{bmatrix} \tag{C6}$$

where the following notations are used as:

$$\varpi = \frac{\lambda - \kappa}{\upsilon p^{'3}\left(M^4 - \eta^4\right)} \tag{C7}$$

$$a_\rho = \frac{p^{'}\left(M^2-\eta^2\right)}{3} + 3\left(\sigma^{'}_\rho - p^{'}\right) \tag{C8}$$

$$a_\omega = \frac{p^{'}\left(M^2-\eta^2\right)}{3} + 3\left(\sigma^{'}_\omega - p^{'}\right) \tag{C9}$$

$$a_w = \frac{p^{'}\left(M^2-\eta^2\right)}{3} + 3\left(\sigma^{'}_w - p^{'}\right) \tag{C10}$$

$$a_{\rho\omega} = 3\tau_{\rho\omega} \tag{C11}$$

In addition, the elastic constitutive relation is:

$$\begin{bmatrix} \frac{d\varepsilon_\rho^e}{dR} \\ \frac{d\varepsilon_\omega^e}{dR} \\ \frac{d\varepsilon_w^e}{dR} \\ \frac{d\varepsilon_{\rho\omega}^e}{dR} \end{bmatrix} = \begin{bmatrix} \frac{1}{2G(1+\mu)} & -\frac{\mu}{2G(1+\mu)} & -\frac{\mu}{2G(1+\mu)} & 0 \\ -\frac{\mu}{2G(1+\mu)} & \frac{1}{2G(1+\mu)} & -\frac{\mu}{2G(1+\mu)} & 0 \\ -\frac{\mu}{2G(1+\mu)} & -\frac{\mu}{2G(1+\mu)} & \frac{1}{2G(1+\mu)} & 0 \\ 0 & 0 & 0 & \frac{1}{2G} \end{bmatrix} \begin{bmatrix} \frac{d\sigma_\rho^{'}}{dR} \\ \frac{d\sigma_\omega^{'}}{dR} \\ \frac{d\sigma_w^{'}}{dR} \\ \frac{d\tau_{\rho\omega}}{dR} \end{bmatrix} \tag{C12}$$

where $G$ is shear modulus and $\mu$ is Poisson's ratio.

Subsequently, the elastic-plastic constitutive relation is:

$$\begin{bmatrix} \dfrac{d\varepsilon_\rho}{dR} \\ \dfrac{d\varepsilon_\omega}{dR} \\ \dfrac{d\varepsilon_w}{dR} \\ \dfrac{d\varepsilon_{\rho\omega}}{dR} \end{bmatrix} = \begin{bmatrix} C_{11} & C_{12} & C_{13} & C_{14} \\ C_{21} & C_{22} & C_{23} & C_{24} \\ C_{31} & C_{32} & C_{33} & C_{34} \\ C_{41} & C_{42} & C_{43} & C_{44} \end{bmatrix} \begin{bmatrix} \dfrac{d\sigma_\rho^{'}}{dR} \\ \dfrac{d\sigma_\omega^{'}}{dR} \\ \dfrac{d\sigma_w^{'}}{dR} \\ \dfrac{d\tau_{\rho\omega}}{dR} \end{bmatrix} \tag{C13}$$

where

$$C_{11} = \varpi a_\rho^2 + \frac{1}{2G(1+\mu)},\ C_{12} = \varpi a_\rho a_y - \frac{\mu}{2G(1+\mu)},\ C_{13} = \varpi a_\rho a_w - \frac{\mu}{2G(1+\mu)},\ C_{14} = \varpi a_\rho a_{\rho\omega} \tag{C14}$$

$$C_{21} = \varpi a_\omega a_\rho - \frac{\mu}{2G(1+\mu)}, C_{22} = \varpi a_\omega^2 + \frac{\mu}{2G(1+\mu)},\ C_{23} = \varpi a_\omega a_w - \frac{\mu}{2G(1+\mu)},\ C_{24} = \varpi a_\omega a_{\rho\omega} \tag{C15}$$

$$C_{31} = \varpi a_w a_\rho - \frac{\mu}{2G(1+\mu)}, C_{32} = \varpi a_w a_\omega - \frac{\mu}{2G(1+\mu)},\ C_{33} = \varpi a_w^2 + \frac{\mu}{2G(1+\mu)},\ C_{34} = \varpi a_w a_{\rho\omega} \tag{C16}$$

$$C_{41} = \varpi a_{\rho\omega} a_\rho,\ C_{42} = \varpi a_{\rho\omega} a_\omega, C_{43} = \varpi a_{\rho\omega} a_w,\ C_{44} = \varpi a_{\rho\omega}^2 + \frac{1}{2G} \tag{C17}$$

## APPENDIX D: TRANSFORMATION OF STRESS AND STRAIN FROM PHASE PLANE TO PHYSICAL PLANE

The transformation between different coordinate systems for stress and strain can be summarized as:

$$S_{p\_\text{phase}} = S_{c\_\text{physical}} e^{-2i\lambda} \tag{D1}$$

$$S_{p\_\text{physical}} = S_{c\_\text{physical}} e^{-2i\theta} \tag{D2}$$

$$e^{-2i\lambda} = \left\{ \frac{\overline{\zeta}}{\rho} \frac{\overline{z^{'}(\zeta)}}{\left|z^{'}(\zeta)\right|} \right\}^2 = \frac{\overline{\zeta}}{\zeta} \frac{\overline{z^{'}(\zeta)}}{z^{'}(\zeta)} \tag{D3}$$

$$e^{-2i\theta} = \left\{ \left|z(\zeta)\right| / z(\zeta) \right\}^2 = \overline{z(\zeta)} / z(\zeta) \tag{D4}$$

where $S_{p\_\text{phase}}\left(\sigma_\rho - \sigma_\omega + 2i\tau_{\rho\omega}\right.$ or $\left.\varepsilon_\rho - \varepsilon_\omega + 2i\varepsilon_{\rho\omega}\right)$ defines the complex stress or strain components in polar coordinates in the phase plane, $S_{p\_\text{physical}}\left(\sigma_r-\sigma_\theta+2i\tau_{r\theta}\text{ or }\varepsilon_r-\varepsilon_\theta+2i\varepsilon_{r\theta}\right)$ is the complex stress or strain components in polar coordinates in the physical plane, and $S_{c\_\text{physical}}\left(\sigma_x-\sigma_y+2i\tau_{xy}\text{ or }\varepsilon_x-\varepsilon_y+2i\varepsilon_{xy}\right)$ is the complex stress or strain components Cartesian coordinates in the physical plane.

## APPENDIX E: EQUILIBRIUM EQUATION IN ORTHOGONAL CURVILINEAR COORDINATE SYSTEM

Following Saada (2013), the stress equilibrium equation in an orthogonal curvilinear coordinate system can be expressed as:

$$\begin{aligned}&\frac{\partial}{\partial y_1}\left(\sigma_{11}h_2h_3\right)+\frac{\partial}{\partial y_2}\left(\sigma_{21}h_1h_3\right)+\frac{\partial}{\partial y_3}\left(\sigma_{31}h_1h_2\right)+\sigma_{12}h_3\frac{\partial h_1}{\partial y_2}\\&+\sigma_{13}h_2\frac{\partial h_1}{\partial y_3}-\sigma_{22}h_3\frac{\partial h_2}{\partial y_1}-\sigma_{33}h_2\frac{\partial h_3}{\partial y_1}+h_1h_2h_3\left(F_1-\rho_sA_1\right)=0\end{aligned}\tag{E1}$$

$$\begin{aligned}&\frac{\partial}{\partial y_1}\left(\sigma_{12}h_2h_3\right)+\frac{\partial}{\partial y_2}\left(\sigma_{22}h_1h_3\right)+\frac{\partial}{\partial y_3}\left(\sigma_{32}h_1h_2\right)+\sigma_{23}h_1\frac{\partial h_2}{\partial y_3}\\&+\sigma_{21}h_3\frac{\partial h_2}{\partial y_1}-\sigma_{33}h_1\frac{\partial h_3}{\partial y_2}-\sigma_{11}h_3\frac{\partial h_1}{\partial y_2}+h_1h_2h_3\left(F_2-\rho_sA_2\right)=0\end{aligned}\tag{E2}$$

$$\begin{aligned}&\frac{\partial}{\partial y_1}\left(\sigma_{13}h_2h_3\right)+\frac{\partial}{\partial y_2}\left(\sigma_{23}h_1h_3\right)+\frac{\partial}{\partial y_3}\left(\sigma_{33}h_1h_2\right)+\sigma_{31}h_2\frac{\partial h_3}{\partial y_1}\\&+\sigma_{32}h_1\frac{\partial h_3}{\partial y_2}-\sigma_{11}h_2\frac{\partial h_1}{\partial y_3}-\sigma_{22}h_1\frac{\partial h_2}{\partial y_3}+h_1h_2h_3\left(F_3-\rho_sA_3\right)=0\end{aligned}\tag{E3}$$

where $\mathbf{y} = (y_1, y_2, y_3)$ is a three-dimensional vector in an orthogonal curvilinear coordinate system, $\rho_s$ is the soil density, $A_i$ and $F_i$ ($i=1,2,3$) define the acceleration and body force in the $i$ direction, respectively, $h_i$ is the scale factor and it is related to the metric coefficient $g_i$ ($h_i^2$). The expressions for $g_i$ is:

$$g_i=\left|\mathbf{x}\right|^2=\left(\frac{\partial x_1}{\partial y_i}\right)^2+\left(\frac{\partial x_2}{\partial y_i}\right)^2+\left(\frac{\partial x_3}{\partial y_i}\right)^2\tag{E4}$$

where $\mathbf{x} = (x_1, x_2, x_3)$ is a three-dimensional vector in the Cartesian coordinate system. For a two-dimensional plane strain problem, the expression for $g_i$ ($i = \rho, \omega, w$) reduces to:

$$g_{\rho} = \left(\frac{\partial x}{\partial \rho}\right)^2 + \left(\frac{\partial y}{\partial \rho}\right)^2 \tag{E5}$$

$$g_{\omega} = \left(\frac{\partial x}{\partial \omega}\right)^2 + \left(\frac{\partial y}{\partial \omega}\right)^2 \tag{E6}$$

$$g_{w} = \left(\frac{\partial x}{\partial w}\right)^2 + \left(\frac{\partial y}{\partial w}\right)^2 + \left(\frac{\partial w}{\partial w}\right)^2 = 1 \tag{E7}$$

For the conformal mapping coordinate system, Equations (E5) and (E6) can be written in complex variable form as:

$$g_{\rho} = \left|\frac{\partial z(\zeta)}{\partial \rho}\right|^2 = \left|\frac{\partial z(\zeta)}{\partial \zeta}\frac{\partial \zeta}{\partial \rho}\right|^2 = \left|z^{'}(\zeta)\right|^2 \tag{E8}$$

$$g_{\omega} = \left|\frac{\partial z(\zeta)}{\partial \omega}\right|^2 = \left|\frac{\partial z(\zeta)}{\partial \zeta}\frac{\partial \zeta}{\partial \omega}\right|^2 = \rho^2\left|z^{'}(\zeta)\right|^2 \tag{E9}$$

Subsequently, the scale factor $h_i$ can be expressed as:

$$h_{\rho} = \left|z^{'}(\zeta)\right| = RH(\rho,\omega) \tag{E10}$$

$$h_{\omega} = \rho\left|z^{'}(\zeta)\right| = R\rho H(\rho,\omega) \tag{E11}$$

$$h_{w} = 1 \tag{E12}$$

Considering only force balance in the expansion (horizontal) plane for plane strain conditions, the acceleration and body force are ignored such that Equations (E1) and (E2) can be simplified as:

$$\frac{\partial \sigma_{\rho}}{\partial \rho} + \frac{1}{\rho}\frac{\partial \tau_{\rho\omega}}{\partial \omega} + \left(1 + \rho\frac{H_{\rho}}{H}\right)\frac{(\sigma_{\rho} - \sigma_{\omega})}{\rho} + 2\frac{H_{\omega}}{H}\frac{\tau_{\rho\omega}}{\rho} = 0 \tag{E13}$$

$$\frac{1}{\rho}\frac{\partial \sigma_{\omega}}{\partial \omega} + \frac{\partial \tau_{\rho\omega}}{\partial \rho} - \frac{H_{\omega}}{H}\frac{(\sigma_{\rho} - \sigma_{\omega})}{\rho} + 2\left(1 + \rho\frac{H_{\rho}}{H}\right)\frac{\tau_{\rho\omega}}{\rho} = 0 \tag{E14}$$

The function $H(\rho,\omega)$ can be written as:

$$H(\rho,\omega) = \frac{1}{R}\left|z^{'}(\zeta)\right| = \frac{1}{R}\sqrt{z^{'}(\zeta)\overline{z^{'}(\zeta)}} \tag{E15}$$

The derivatives of $H\left(\rho,\omega\right)$ with respect to $\rho$ and $\omega$ can be derived as:

$$H_{\rho}=\frac{\partial H}{\partial \rho}=\frac{\partial H}{\partial z^{'}}\frac{\partial z^{'}}{\partial \zeta}\frac{\partial \zeta}{\partial \rho}+\frac{\partial H}{\partial \overline{z^{'}}}\frac{\partial \overline{z^{'}}}{\partial \overline{\zeta}}\frac{\partial \overline{\zeta}}{\partial \rho}=\frac{1}{2R}\left[z^{"}\sigma\sqrt{\overline{z^{'}}/z^{'}}+\overline{z^{"}}\sigma^{-1}\sqrt{z^{'}/\overline{z^{'}}}\right]=\frac{1}{R}\mathrm{Re}\left[z^{"}\sqrt{\overline{z^{'}}/z^{'}}\right] \tag{E16}$$

$$H_{\omega}=\frac{\partial H}{\partial \omega}=\frac{\partial H}{\partial z^{'}}\frac{\partial z^{'}}{\partial \zeta}\frac{\partial \zeta}{\partial \omega}+\frac{\partial H}{\partial \overline{z^{'}}}\frac{\partial \overline{z^{'}}}{\partial \overline{\zeta}}\frac{\partial \overline{\zeta}}{\partial \omega}=\frac{1}{2R}\left[i\rho\sigma z^{"}\sqrt{\overline{z^{'}}/z^{'}}-i\rho\sigma^{-1}\overline{z^{"}}\sqrt{z^{'}/\overline{z^{'}}}\right]=\frac{1}{R}\mathrm{Re}\left[i\rho\sigma z^{"}\sqrt{\overline{z^{'}}/z^{'}}\right] \tag{E17}$$

$z^{'}$ and $z^{"}$ are the first and second derivatives of the conformal mapping function with respect to $\zeta$ .

## DATA AVAILABILITY STATEMENT

All data, models, or code that support the findings of this study are available from the corresponding author upon reasonable request.


## ACKNOWLEDGEMENTS

The work was supported by the National Natural Science Foundation of China, Grant/Award Number 51978105 and 52027812; the Chongqing Science Foundation for Distinguished Young Scholars, Grant/Award Number: cstc2021jcyj-jqX0017 and the Chongqing Youth Top Talent Plan, Grant/Award Number: cstc2021ycjh-bgzxm0132. The second author is funded by the Royal Academy of Engineering under the Research Fellowship Scheme.


## REFERENCES


Baligh, M. M. (1985). Strain path method. Journal of Geotechnical Engineering, 111(9), 1108-1136.

Basu, D., & Salgado, R. (2008). Analysis of laterally loaded piles with rectangular cross sections embedded in layered soil. International Journal for Numerical and Analytical Methods in Geomechanics, 32(7), 721-744.

Chen, S. L., and Abousleiman, Y. N. 2012. Exact undrained elasto-plastic solution for cylindrical cavity expansion in modified Cam Clay soil. Geotechnique, 62(5):447-456.

Chen, S. L., and Abousleiman, Y. N. 2013. Exact drained solution for cylindrical cavity expansion in modified Cam Clay soil. Geotechnique, 63(6):510-517.

Chen, S. L., and Liu, K. 2019. Undrained cylindrical cavity expansion in anisotropic undrained soils. Geotechnique, 69(3):189-202.

Chen, H., Li, L., & Li, J. (2020). Elastoplastic solutions for cylindrical cavity expansion in unsaturated soils. Computers and Geotechnics, 123, 103569.

Collins, I. F., and Stimpson, J. R. 1994. Similarity solutions for drained and undrained cavity expansions in soils. Geotechnique, 44(1):21-34.

Currie IG. (2012). Fundamental Mechanics of Fluids. New York, USA: CRC Press.

Ghandeharioon, A., Indraratna, B., & Rujikiatkamjorn, C. (2010). Analysis of soil disturbance associated with mandrel-driven prefabricated vertical drains using an elliptical cavity expansion theory. International Journal of Geomechanics, 10(2), 53-64.

Gibson, R. E., and Anderson, W. F. 1961. In situ measurement of soil properties with the pressuremeter. Civ. Engng Public Works Rev, 56(658):615-618.

Mantaras, F. M., and Schnaid, F. 2002. Cylindrical cavity expansion in dilatant cohesive-frictional materials. Geotechnique, 52(5):337-348.

Muskhelishvili, N. I. (1954). Some basic problems of the mathematical theory of elasticity, P. Noordhoff, Groningen, Netherlands.

Li, C., & Zou, J. F. (2019). Closed-form solution for undrained cavity expansion in anisotropic soil mass based on spatially mobilized plane failure criterion. International Journal of Geomechanics, 19(7), 04019075.

Liu, H., Zhou, H., & Kong, G. (2014). XCC pile installation effect in soft soil ground: a simplified analytical model. Computers and Geotechnics, 62, 268-282.

Liu, H., Zhou, H., & Kong, G. (2016). Upper-bound solution for flat cavity expansion model. Journal of

Engineering Mechanics, 142(7), 04016035.

Liu, F., Yi, J., Cheng, P., & Yao, K. (2020). Numerical simulation of set-up around shaft of XCC pile in clay. Geomechanics and Engineering, 21(5), 489-501.

Liu, H., Zhou, H., Wang, Z., & Li, X. (2021). Theoretical Solution for Cavity Expansion in Crushable Soil. International Journal of Geomechanics, 21(7), 04021098.

Marchetti, S. (1980). In situ tests by flat dilatometer. Journal of the Geotechnical Engineering Division, 106(3), 299-321.

Mo, P. Q., Marshall, A. M., & Yu, H. S. (2017). Interpretation of cone penetration test data in layered soils using cavity expansion analysis. Journal of Geotechnical and Geoenvironmental Engineering, 143(1), 04016084.

Saada, A. S. (2013). Elasticity: theory and applications. Elsevier.

Seo, H., Basu, D., Prezzi, M., & Salgado, R. (2009). Load-settlement response of rectangular and circular piles in multilayered soil. Journal of Geotechnical and Geoenvironmental Engineering, 135(3), 420-430.

Shuttle, D. 2007. Cylindrical cavity expansion and contraction in Tresca soil. Geotechnique, 57(3): 305-308.

Sun, G., Kong, G., Liu, H., & Amenuvor, A. C. (2017). Vibration velocity of X-section cast-in-place concrete (XCC) pile–raft foundation model for a ballastless track. Canadian Geotechnical Journal, 54(9), 1340-1345.

Wang, C. L., Zhou, H., Liu, H. L., & Ding, X. M. (2019). Analysis of undrained spherical cavity expansion in modified Cam Clay of finite radial extent. European Journal of Environmental and Civil Engineering, 1-12.

Wood DM. (1990). Soil behaviour and undrained soil mechanics. Cambridge university press.

Zhou, H., Liu, H., Kong, G., & Cao, Z. (2014). Analytical solution for pressure-controlled elliptical cavity expansion in elastic–perfectly plastic soil. Geotechnique letters, 4(2), 72-78.

Zhou, H., Kong, G., Li, P., & Liu, H. (2016). Flat cavity expansion: theoretical model and application to the interpretation of the flat dilatometer test. Journal of Engineering Mechanics, 142(1), 04015058.

Zhou, H., Liu, H., Randolph, M. F., Kong, G., & Cao, Z. (2017a). Experimental and analytical study of X-section cast-in-place concrete pile installation effect. International Journal of Physical Modelling in Geotechnics, 17(2), 103-121.

Zhou, H. (2017b). Complex variable solution for boundary value problem with X-shaped cavity in plane elasticity and its application. Applied Mathematics and Mechanics, 38(9), 1329-1346.

Zhou, H., Kong, G. Q., Liu, H. L., and Laloui, L. 2018a. Similarity solution for cavity expansion in thermoplastic soil. International Journal for Numerical and Analytical Methods in Geomechanics, 42(2):274-294.

Zhou, H., Yuan, J., Liu, H., & Kong, G. (2018b). Analytical model for evaluating XCC pile shaft capacity in soft soil by incorporating penetration effects. Soils and foundations, 58(5), 1093-1112..

Zhou, H., Liu, H., Yuan, J., & Chu, J. (2019). Numerical simulation of XCC pile penetration in undrained clay. Computers and Geotechnics, 106, 18-41.

Zhou, H., Liu, H., Ding, X., & Kong, G. (2020). A p–y curve model for laterally loaded XCC pile in soft clay. Acta Geotechnica, 15(11), 3229-3242.

Zhou, H., Liu, H., Wang, Z., & Ding, X. (2021a). A unified and rigorous solution for quasi-static cylindrical cavity expansion in plasticity constitutive models. Computers and Geotechnics, 135, 104162.

Zhou, H., Liu, H., Wang, Z., & Tong, L. (2021b). Analytical solution for cavity expansion in rate-dependent and strain-softening clay and its application for CPT tests. Journal of Engineering Mechanics, 147(3), 04021004.

Zhou, H., Wang, Z., Liu, H., Shen, H., & Ding, X. (2021c). Undrained cylindrical and spherical cavity expansion in elastic-viscoplastic soils. Canadian Geotechnical Journal.

Zhou, H., Liu, H., Wang, Z. (2021d). A semi-analytical solution for displacement-controlled elliptical cavity expansion in undrained MCC soil. International Journal for Numerical and Analytical Methods in Geomechanics (*Published online* doi.org/10.1002/nag.3302)

**List of Figure Captions**

Figure 1 Definition of N-CCE model

Figure 2 Conformal mapping from (a) an arbitrary non-circular cavity to (b) a unit circular cavity shown in the physical plane (Red and blue lines are isolines of the variables $\rho$ and $\vartheta$ respectively)

Figure 3 Conformal mapping coordinate system (a) circle; (b) ellipse; (c) square; and (d) X-shaped shown in the physical plane(Red and blue lines are isolines of the variables $\rho$ and $\vartheta$ respectively)

Figure 4 Velocity components in the physical ($z$) and phase ($\zeta$) planes

Figure 5 Boundary conditions and finite difference grid for pore water pressure analysis

Figure 6 Comparison of the proposed N-CCE approach with the traditional CCE solution for the development of normalized radial displacement ($u_r/R$) and three strain components ($\varepsilon_r$, $\varepsilon_\theta$, $\varepsilon_{r\theta}$) with normalized radial distance ($r/R$) for a circular cavity

Figure 7 Comparison of the proposed N-CCE approach with Chen & Abousleiman (2012) for the development of normalized radial excess pore pressure at the cavity-soil interface ($\Delta u_a/s_u$) with normalized radial expansion ($R/R_0$) for a circular cavity

Figure 8 Comparison of the proposed solution with Chen & Absouleiman (2012) for the development of effective stress with normalized radial distance based on traditional CCE: (a) $R_{oc}$ = 1; (b) $R_{oc}$ = 10

Figure 9 Comparison of the proposed solution with the Randolph & Wroth (1979) closed-form solutions for the dissipation of normalized excess pore pressure at the interface of a circular cavity with (a) normalized radial distance and (b) dimensionless time

Figure 10 Soil velocity vector field plotted on a normalized *x*-*y* plane caused by the expansion of (a) circular, (b) elliptical, (c) square, and (d) X-shaped cavities

Figure 11 Influence of cavity shape on the distribution of expansion-induced normalized radial displacements with normalized radial distance along different axes of symmetry

Figure 12 Contours of N-CCE calculated maximum soil shear strains plotted on a normalized *x*-*y* plane induced by the expansion of (a) circular, (b) elliptical, (c) square, and (d) X-shaped cavities

Figure 13 Contours of N-CCE calculated soil shear stress plotted on a normalized *x*-*y* plane induced by the expansion of (a) circular, (b) elliptical, (c) square, and (d) X-shaped cavities in BBC

Figure 14 Development of N-CCE calculated normalized effective radial, tangential and vertical stress with normalized radial distance caused by the expansion of (a) circular, (b) elliptical, (c) square, and (d) X-shaped cavities in BBC

Figure 15 Development of N-CCE calculated normalized effective radial, tangential, vertical and shear stress with polar angle caused by the expansion of (a) circular, (b) elliptical, (c) square, and (d) X-shaped cavities in BBC

Figure 16 Contours of N-CCE calculated excess pore pressure caused by the expansion of (a) circular, (b) elliptical, (c) square, and (d) X-shaped cavities in BBC

Figure 17 Radial distribution of N-CCE calculated normalized excess pore pressure surrounding the cavity for different stages of consolidation after cavity expansion for (a) circular, (b) elliptical, (c) square, and (d) X-shaped cavities

Figure 18 Circumferential variation of N-CCE calculated excess pore pressure at the cavity-soil interface for different stages of consolidation after cavity expansion for (a) circular, (b) elliptical, (c) square, and (d) X-shaped cavities

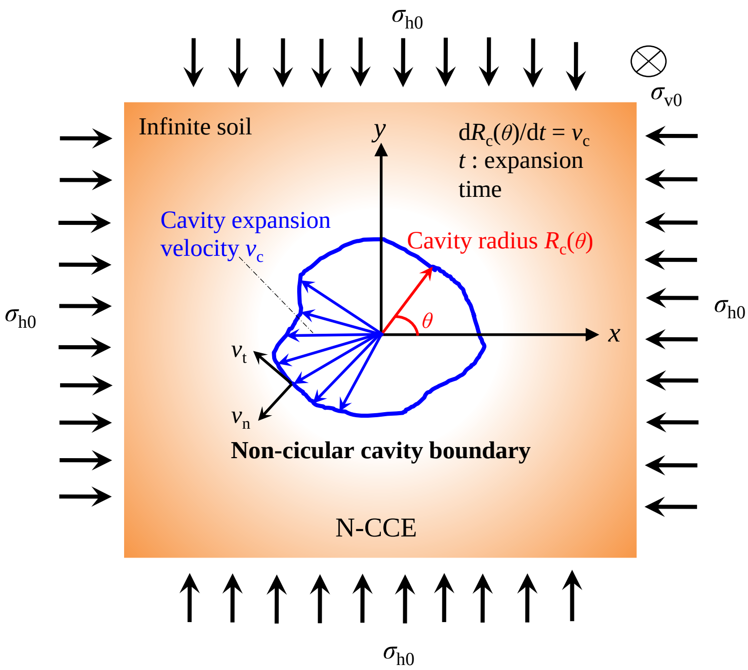


Figure 1 Definition of N-CCE model

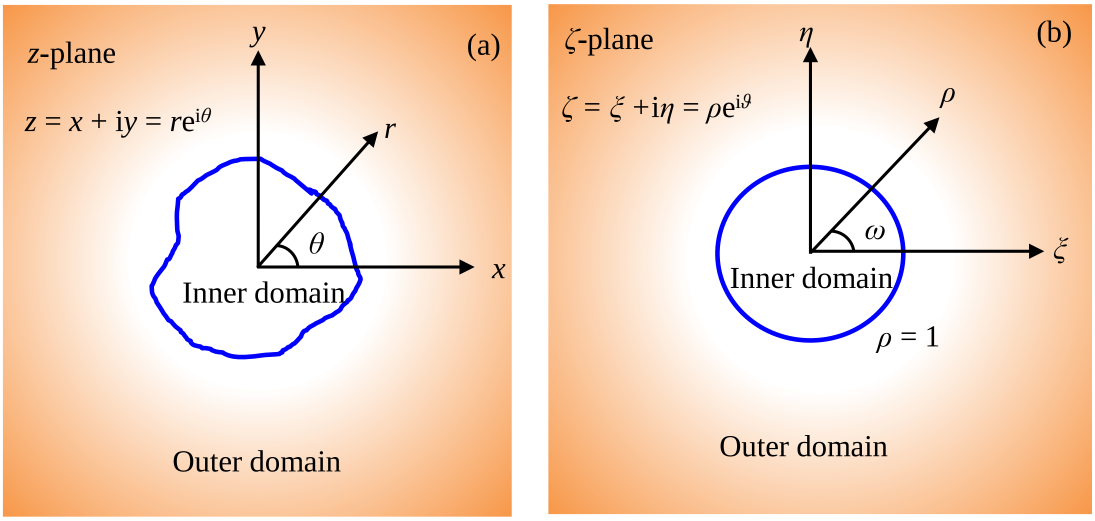


Figure 2 Conformal mapping from (a) an arbitrary non-circular cavity to (b) a unit circular cavity

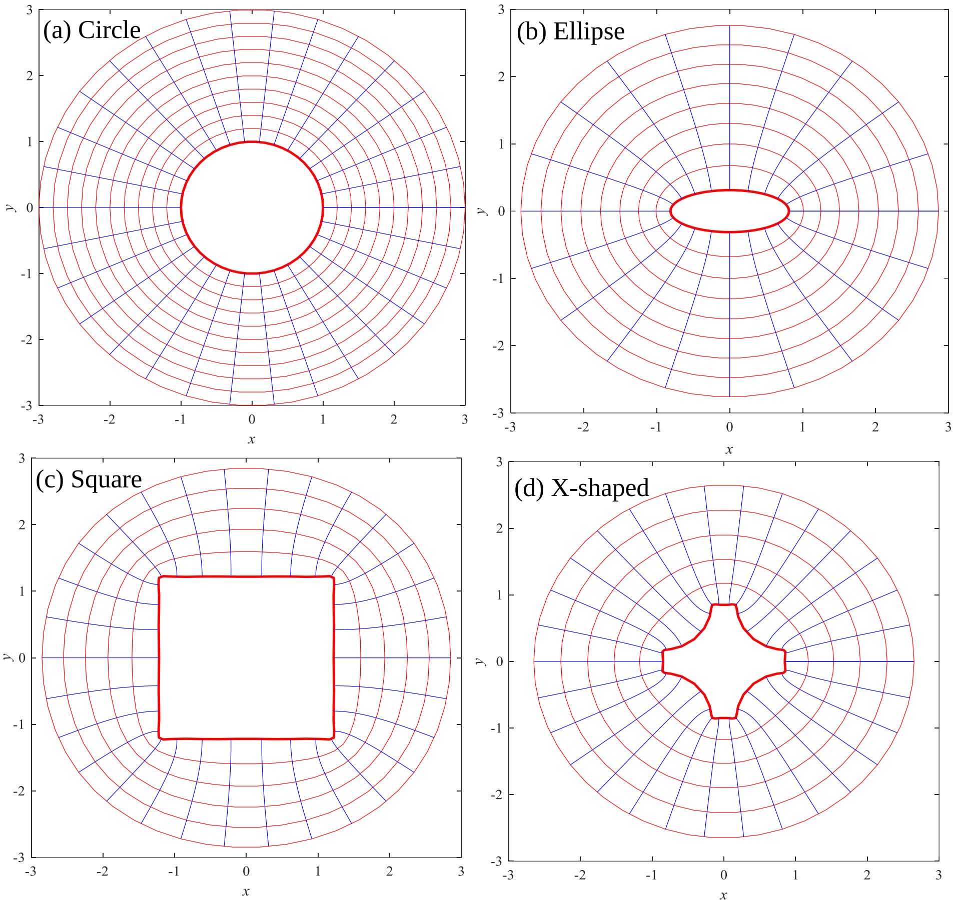


Figure 3 Conformal mapping coordinate system (a) circle; (b) ellipse; (c) square; and (d) X-shaped shown in the physical plane(Red and blue lines are isolines of the variables $\rho$ and $\vartheta$ respectively)

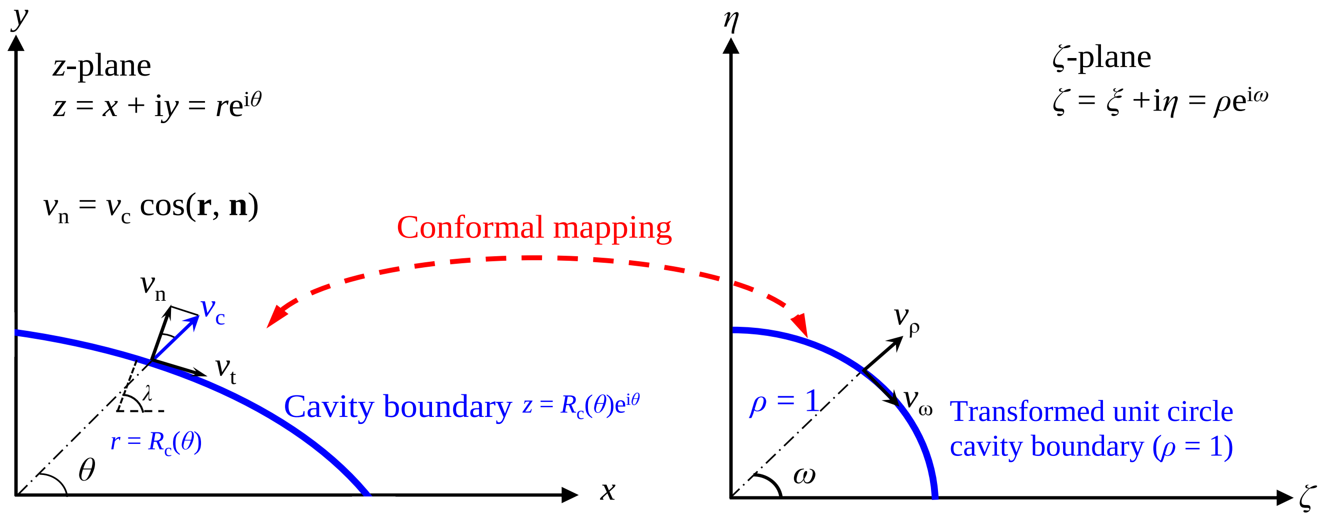


Figure 4 Velocity components in the physical ($z$) and phase ($\zeta$) planes

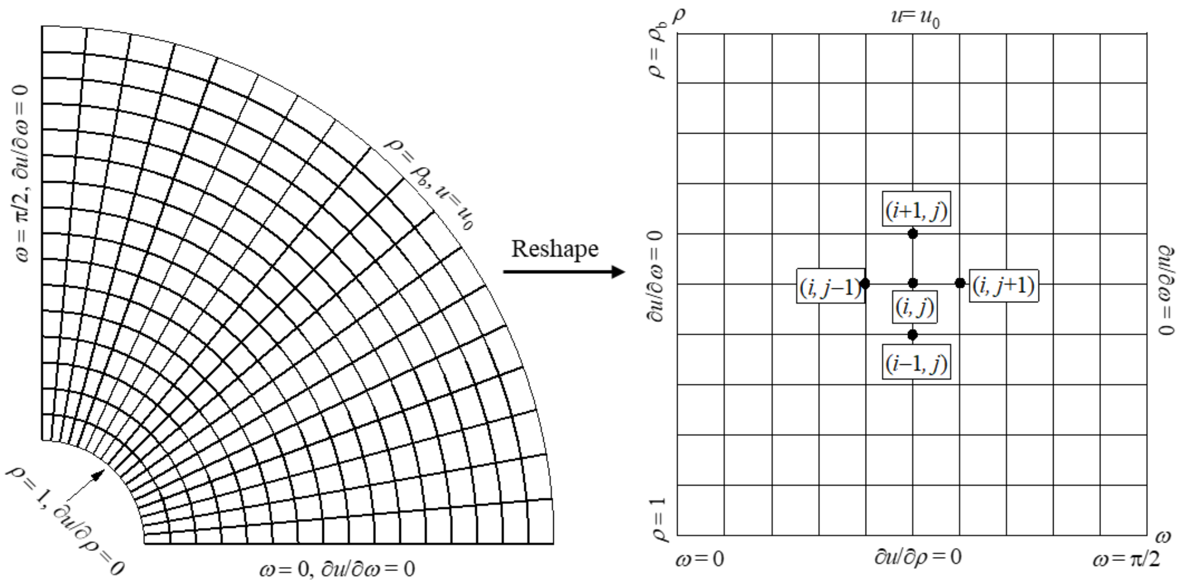


Figure 5 Boundary conditions and finite difference grid for pore water pressure analysis

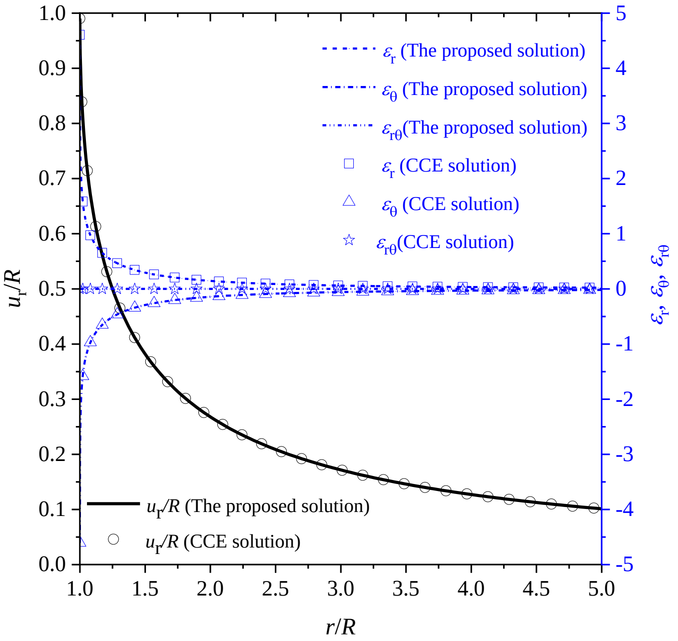


Figure 6 Comparison of the proposed N-CCE approach with the traditional CCE solution for the development of normalized radial displacement ($u_r/R$) and three strain components ($\varepsilon_r$, $\varepsilon_\theta$, $\varepsilon_{r\theta}$) with normalized radial distance ($r/R$) for a circular cavity (See Table 1 for parameters)

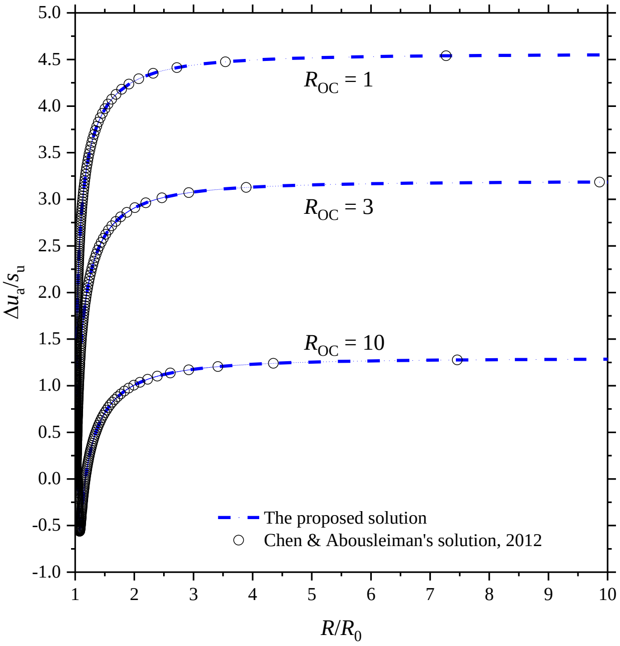


Figure 7 Comparison of the proposed N-CCE approach with Chen & Abousleiman (2012) for the development of normalized radial excess pore pressure at the cavity-soil interface ($\Delta u_a/s_u$) with normalized radial expansion ($R/R_0$) for a circular cavity (See Table 1 for parameters)

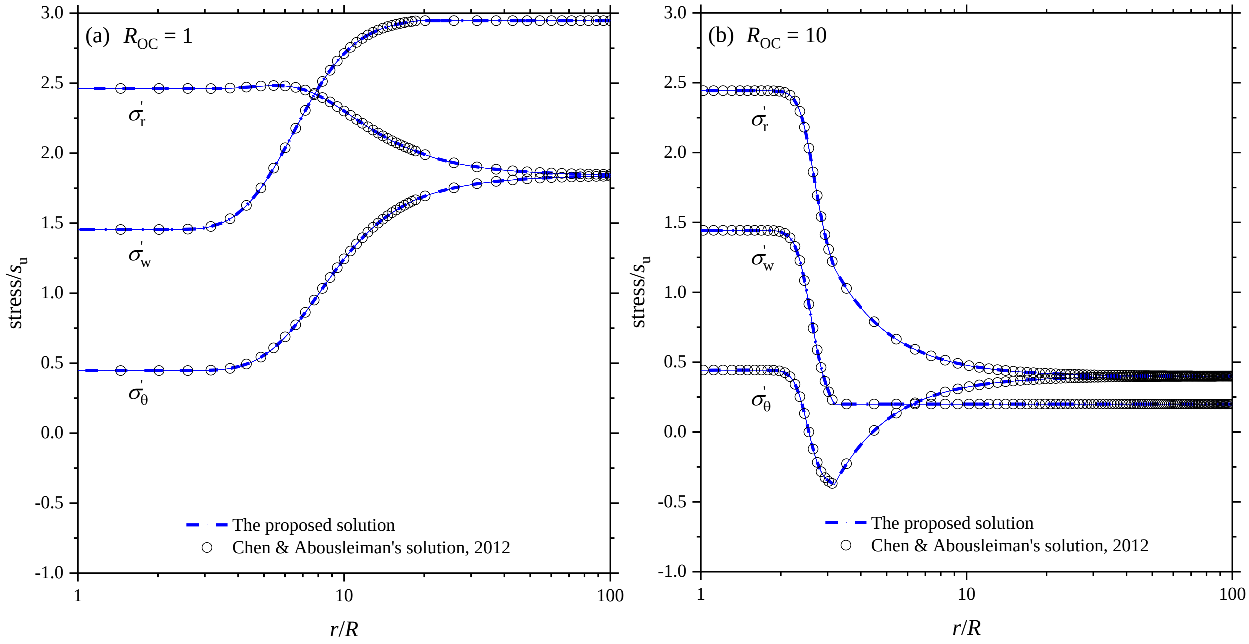


Figure 8 Comparison of the proposed solution with Chen & Absouleiman (2012) for the development of effective stress with normalized radial distance based on traditional CCE: (a) $R_{oc}$ = 1; (b) $R_{oc}$ = 10 (See Table 1 for parameters)

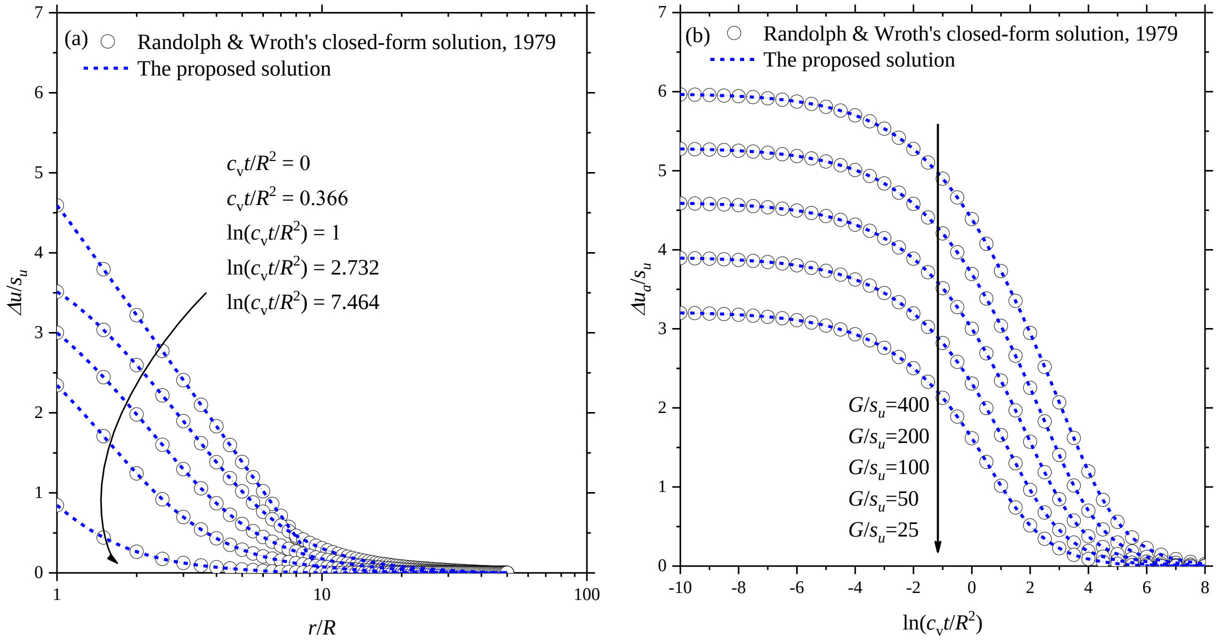


Figure 9 Comparison of the proposed solution with the Randolph & Wroth (1979) closed-form solutions for the dissipation of normalized excess pore pressure at the interface of a circular cavity with (a) normalized radial distance and (b) dimensionless time

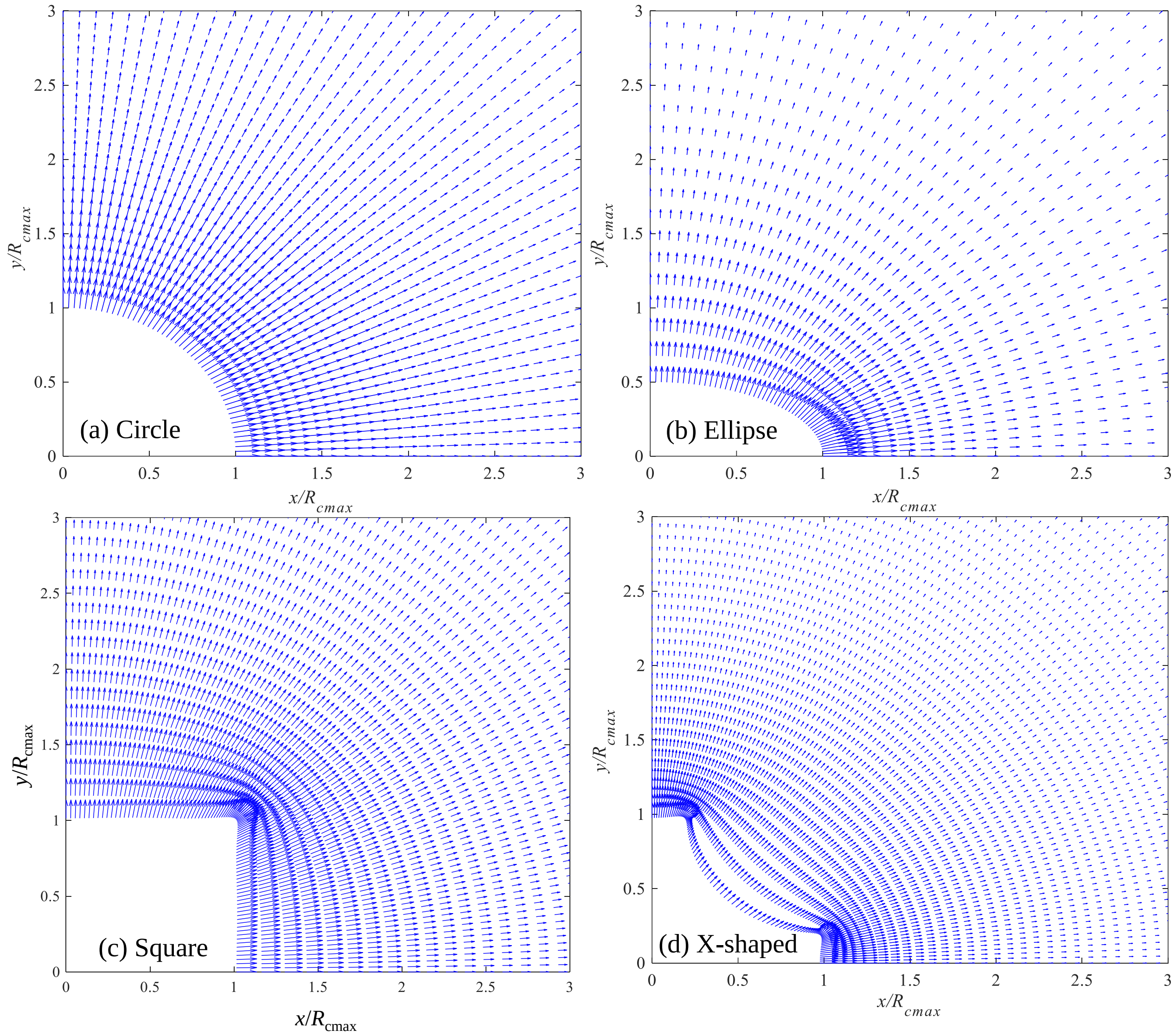


Figure 10 Soil velocity vector field plotted on a normalized *x*-*y* plane caused by the expansion of (a) circular, (b) elliptical, (c) square, and (d) X-shaped cavities

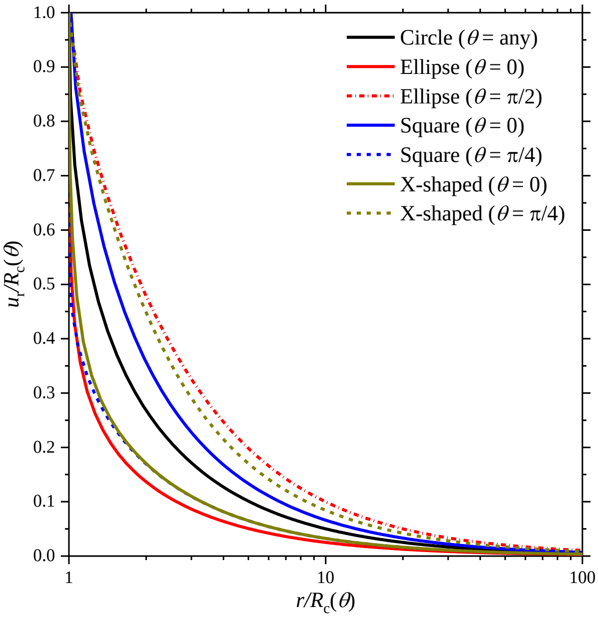


Figure 11 Influence of cavity shape on the distribution of expansion-induced normalized radial displacements with normalized radial distance along different axes of symmetry

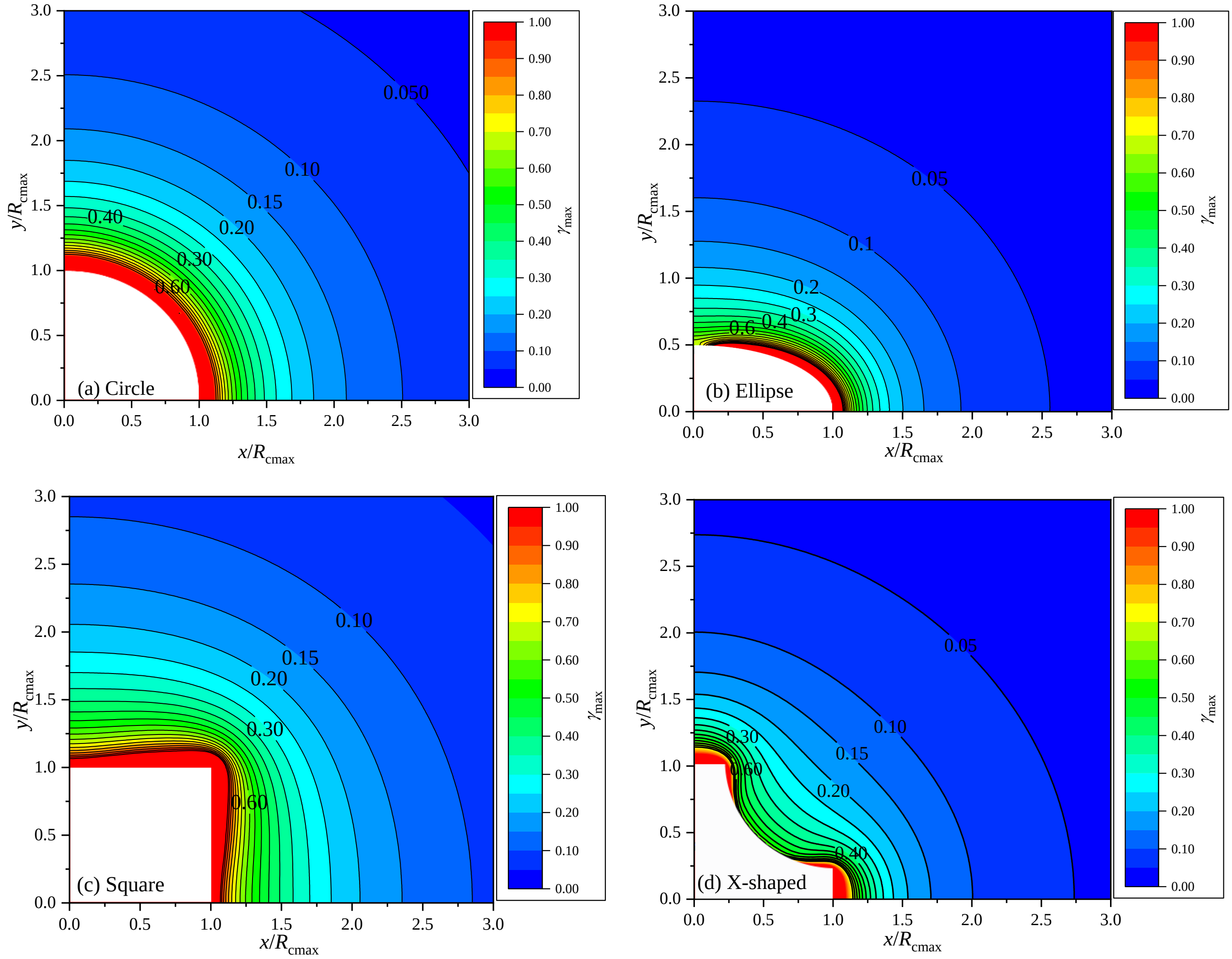


Figure 12 Contours of N-CCE calculated maximum soil shear strains plotted on a normalized *x*-*y* plane induced by the expansion of (a) circular, (b) elliptical, (c) square, and (d) X-shaped cavities

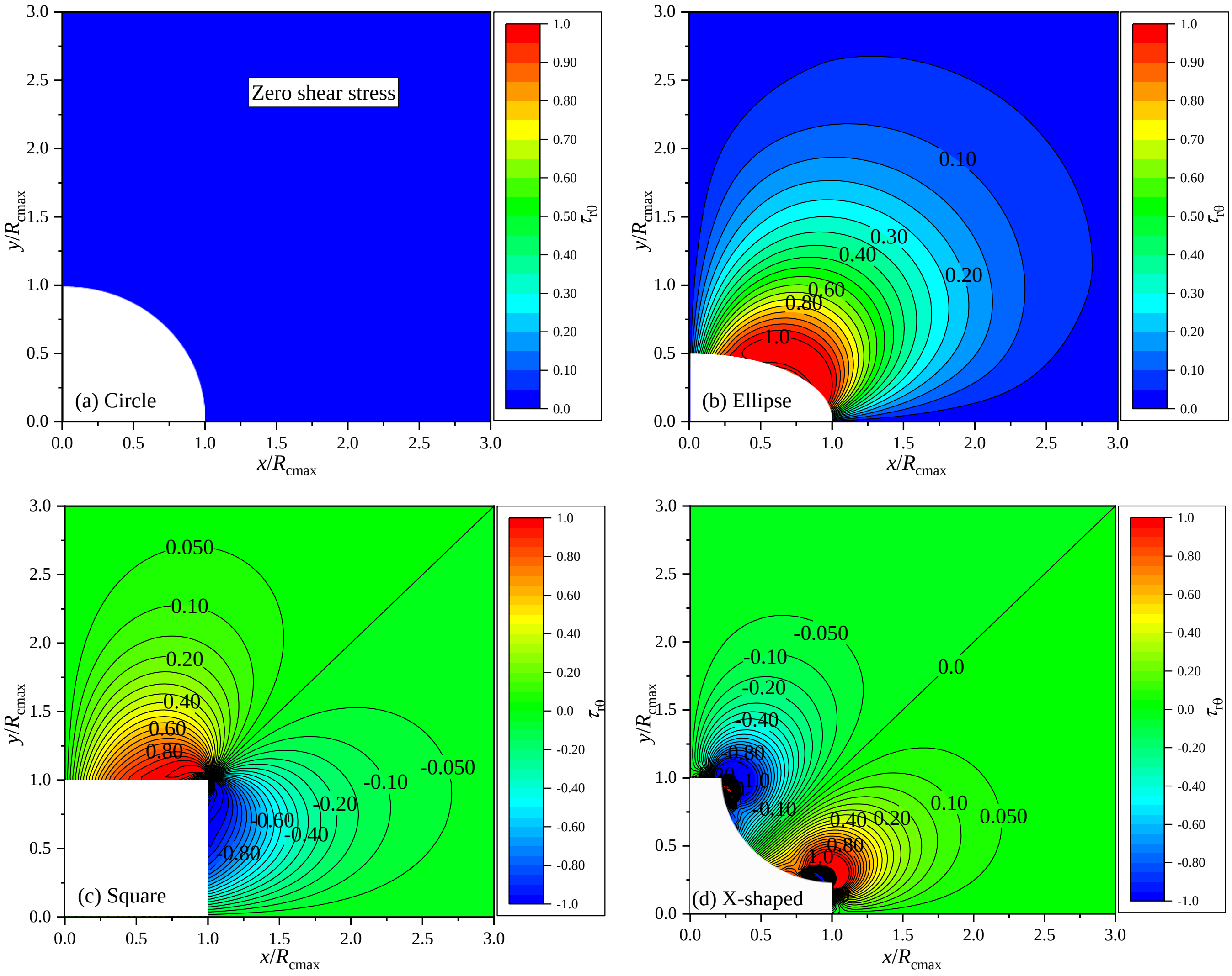


Figure 13 Contours of N-CCE calculated soil shear stress plotted on a normalized *x*-*y* plane induced by the expansion of (a) circular, (b) elliptical, (c) square, and (d) X-shaped cavities in BBC

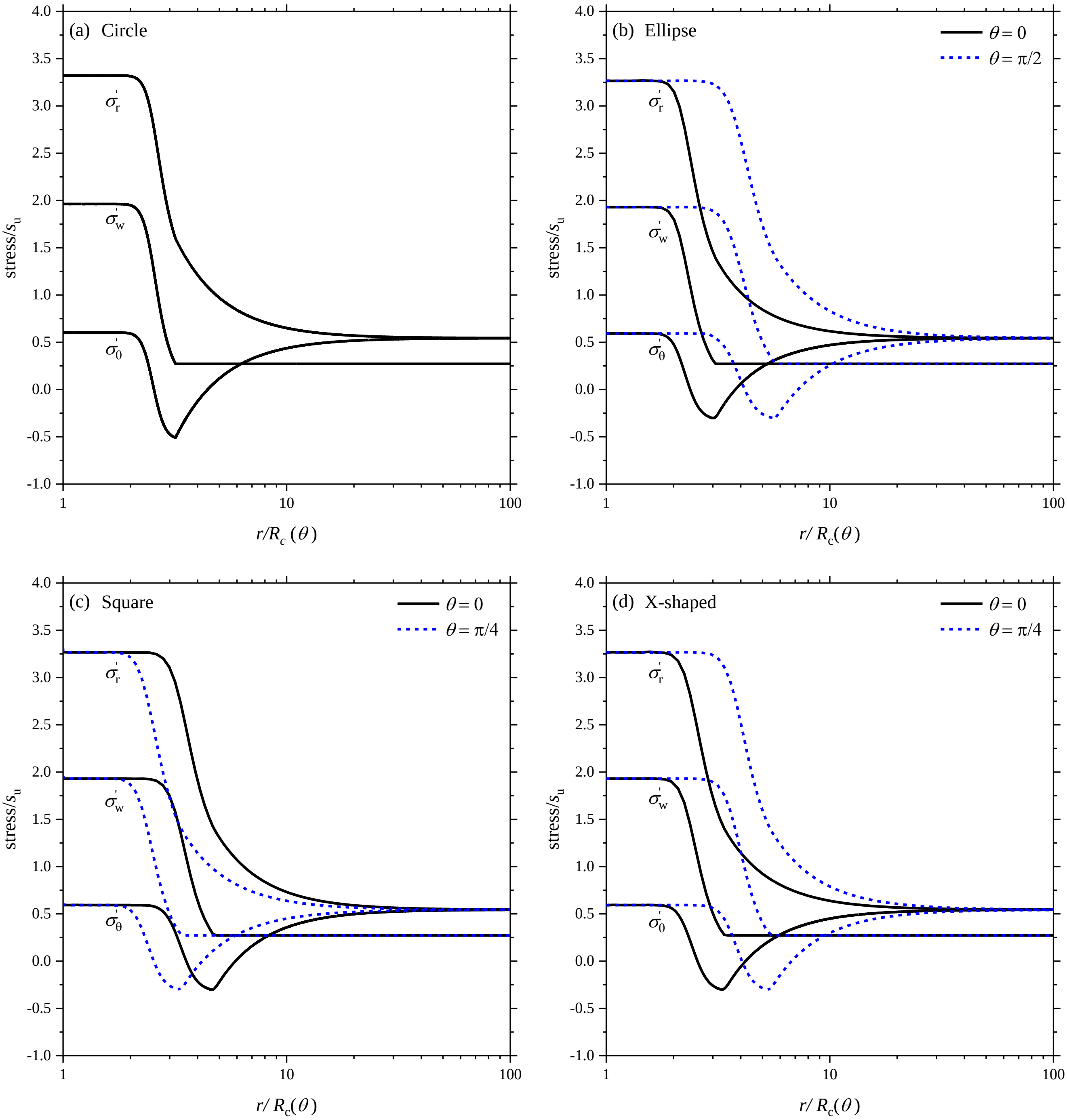


Figure 14 Development of N-CCE calculated normalized effective radial, tangential and vertical stress with normalized radial distance caused by the expansion of (a) circular, (b) elliptical, (c) square, and (d) X-shaped cavities in BBC

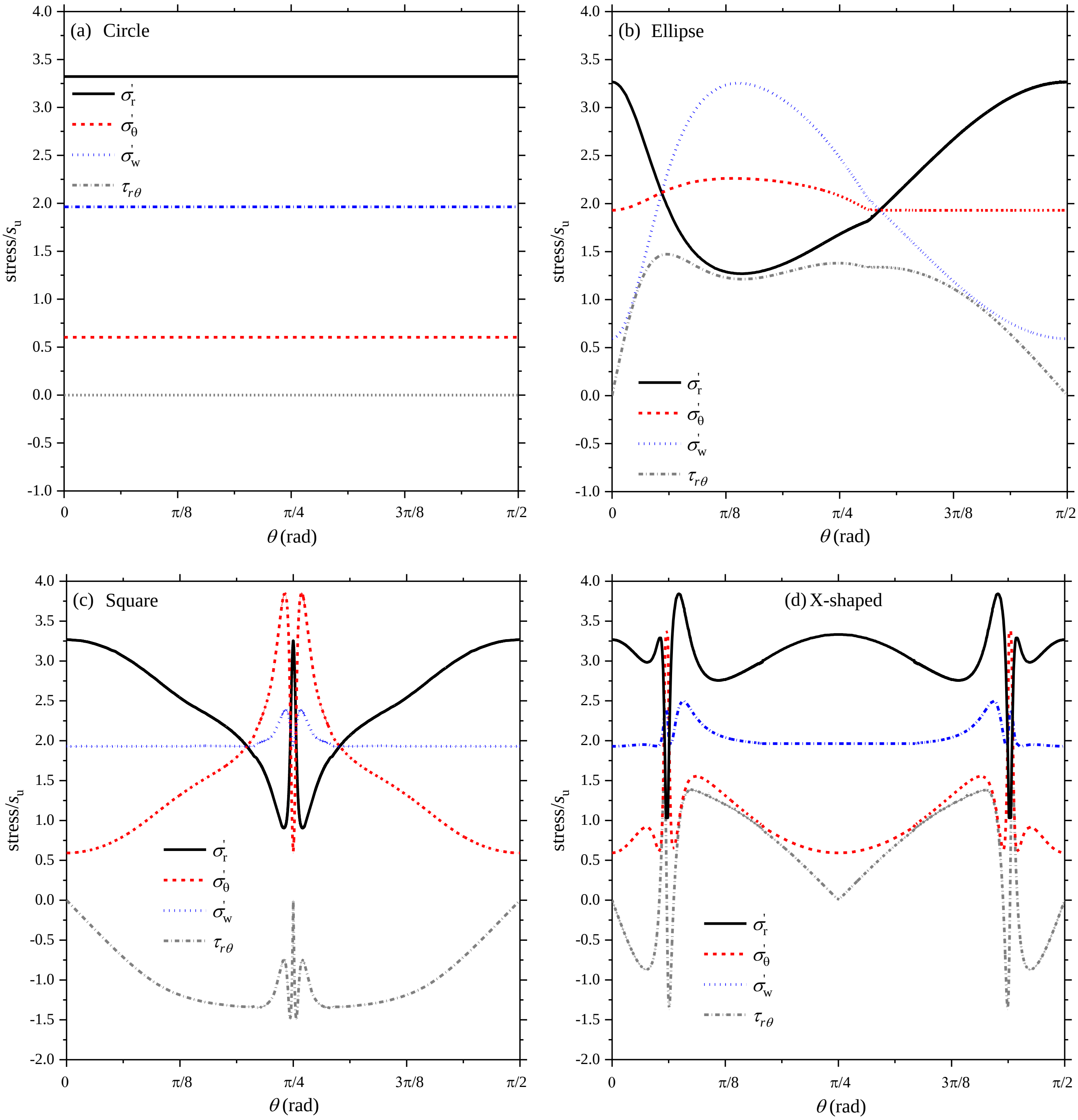


Figure 15 Development of N-CCE calculated normalized effective radial, tangential, vertical and shear stress with polar angle caused by the expansion of (a) circular, (b) elliptical, (c) square, and (d) X-shaped cavities in BBC

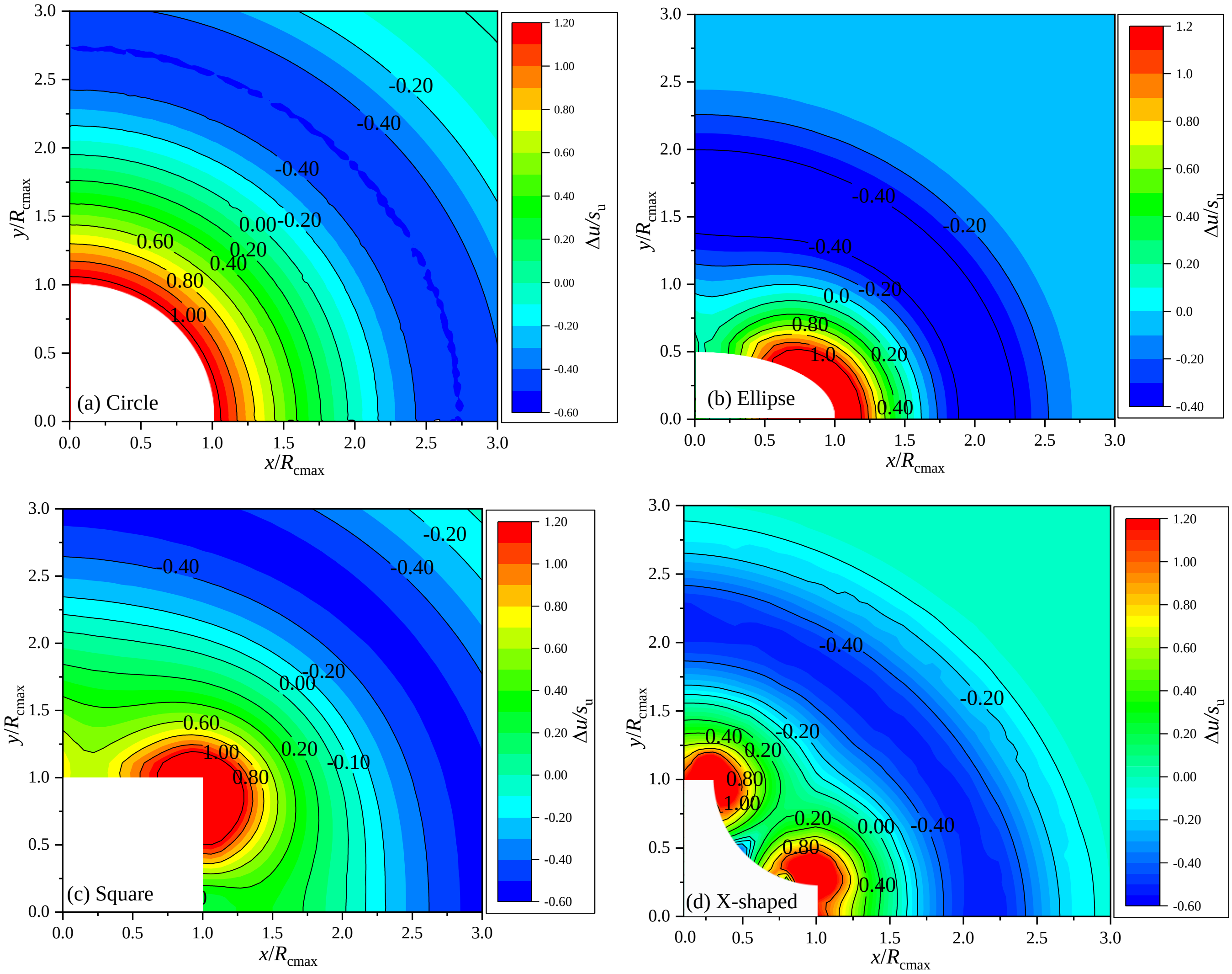

Figure 16 Contours of N-CCE calculated excess pore pressure caused by the expansion of (a) circular, (b) elliptical, (c) square, and (d) X-shaped cavities in BBC

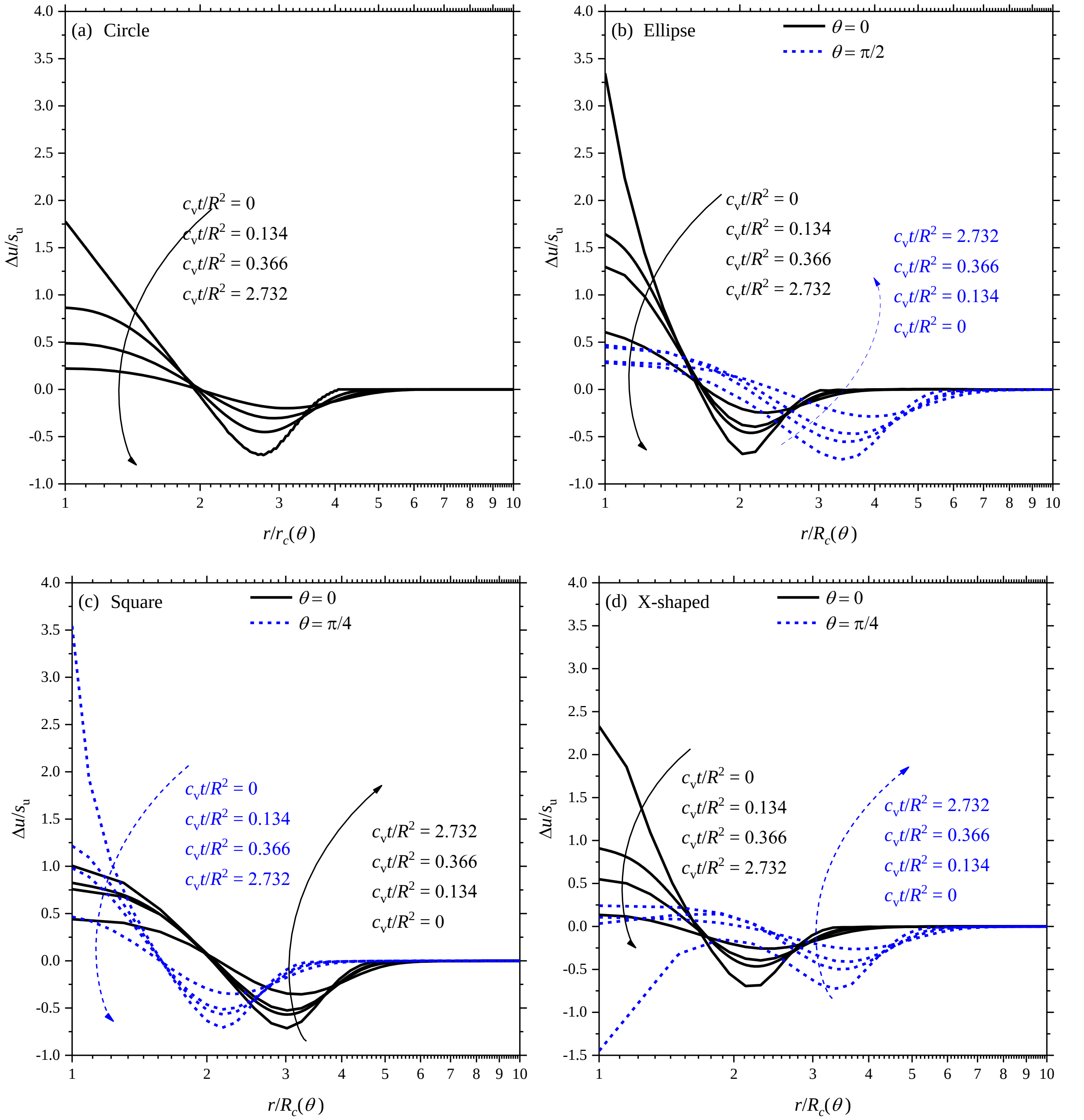


Figure 17 Radial distribution of N-CCE calculated normalized excess pore pressure surrounding the cavity for different stages of consolidation after cavity expansion for (a) circular, (b) elliptical, (c) square, and (d) X-shaped cavities

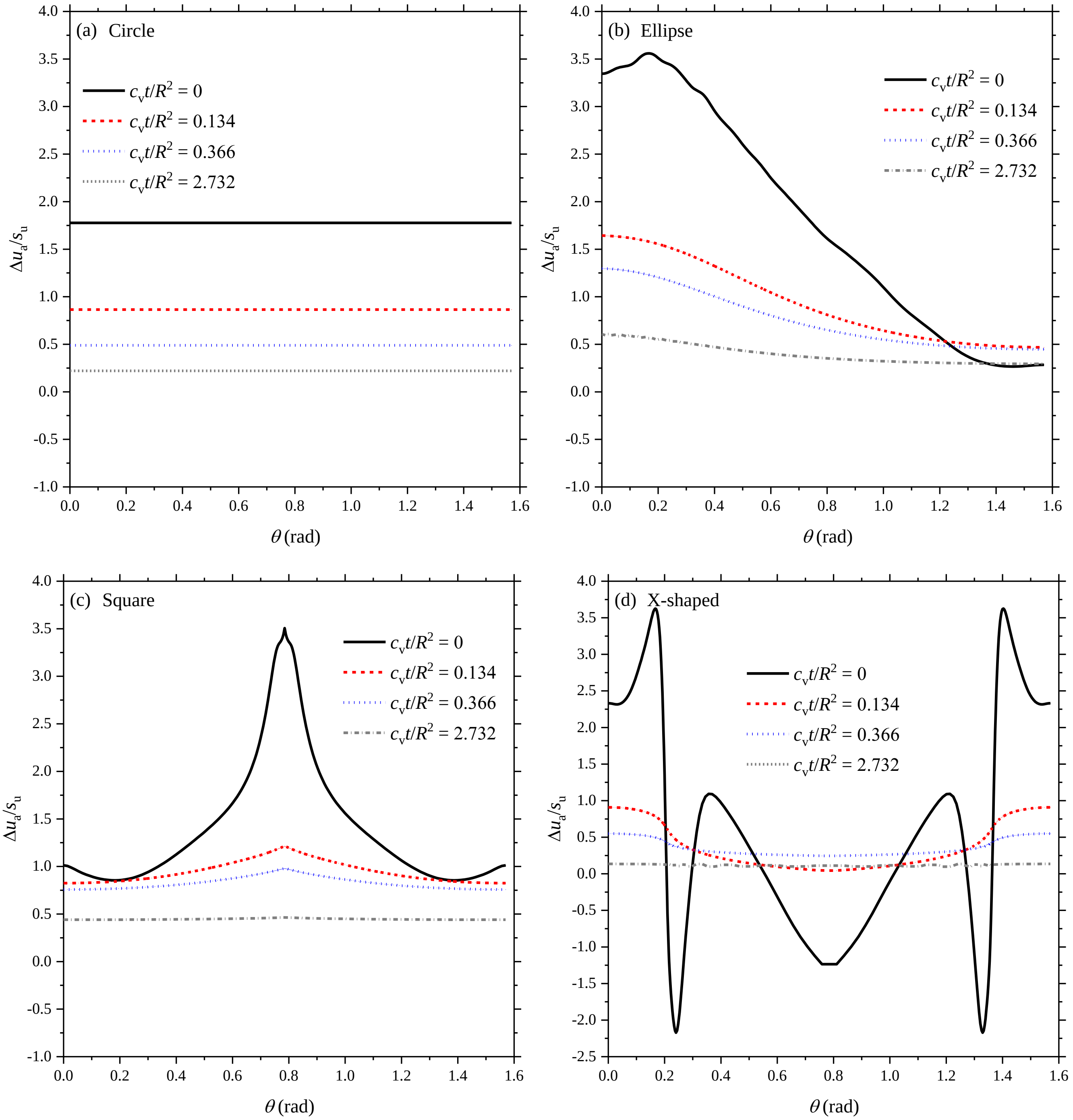


Figure 18 Circumferential variation of N-CCE calculated excess pore pressure at the cavity-soil interface for different stages of consolidation after cavity expansion for (a) circular, (b) elliptical, (c) square, and (d) X-shaped cavities